Granular Dynamics Simulations of Wind-Driven, Broken Ice Fields

By Nathalie Renaut

Department of Civil Engineering and Applied Mechanics

McGill University, Montreal

April, 1995

A Thesis submitted to the Faculty of Graduate Studies and Research in partial fulfillment of the requirements for the degree of Master in Engineering.

ISBN 0-612-19698-4

Abstract

A numerical model is being developed for ice forecasting which is based on a granular dynamics approach. This model is intended to analyse the movements of broken ice fields at the mesoscale; i.e. for length scales of the order of 100 km and time scales of the order of a few days. It will therefore be useful for navigation, for the operation of offshore drilling platforms and for commercial fishing. At the mesoscale, the forces governing the motion of ice floes are: wind drag, water drag, Coriolis force and the contact forces arising from internal collisions. Expressions are developed to evaluate in the most accurate manner the drag exerted by the water and by the wind on individual ice floes by considering non-linear effects. The second aspect of the present work is to modify the inter-particle contacts such that their tangential contribution involves elastic deformation of the ice floes. The effects of an incrementally slipping friction force model are studied for a system where the conditions vary from a quasi-static to a rapid flow regime. Under these circumstances the model is found to adequately reproduce the behaviour of small scale laboratory experiments using aluminum cylinders. Computations performed with tangentially rigid particles yield a system which is very unstable in its behaviour. The analysis of the macroscopic variables, made in order to determine how a broken ice field is affected by the shearing effects of the particles, shows that for a rapidly flowing field the elastic contribution to the contact shear force is minor, if not negligible, when one considers long time averages or instantaneous values. It appears from these investigations that attention must be paid to the problem of ice floes flowing under quasi-static or transitional conditions.

Résumé

Un modèle numérique de type dynamique moléculaire est mis au point pour étudier la rhéologie de la banquise fracturée dans les régions nordiques. Ce modèle est utilisé pour faire l'étude à la mésoéchelle, c'est-à-dire pour une échelle de longueur de l'ordre de 100 km et une échelle de temps de l'ordre de deux jours. Il sera utile, entre autres pour la navigation, les opérations des plate-formes pétrolières et la pêche commerciale. Les forces qui régissent le mouvement de la banquise à la mésoéchelle sont: le frottement du vent et de l'eau, la force de Coriolis et les forces de contact dues aux collisions entre particules. Les effets non linéaires du vent et des courants sont étudiés et des équations sont développées pour en tenir compte. Le deuxième aspect de ce travail est d'améliorer la modélisation des contacts inter-particulaires en considérant la déformation élastique dans la direction tangentielle des contacts. Les effets d'un nouveau modèle de force tangentielle qui prend en compte un tel comportement ont été étudiés dans différents cas. Dans un premier temps, la transition entre un régime quasi-statique et un écoulement rapide, à partir d'un empilement de cylindres en aluminium, a été simulée. Les résultats numériques concordent de façon satisfaisante avec les observations expérimentales. Ce n'est cependant pas le cas lorsque la déformation tangentielle des particules n'est pas considérée. Une analyse détaillée d'un écoulement rapide de banquise fracturée est menée par la suite pour observer les effets du cisaillement des particules. Le calcul des variables macroscopiques, moyennées ou instantanées, montre que ces effets sont minimes pour ne pas dire négligeables. D'après ces résultats, il semble qu'une attention particulière devra être portée sur les écoulements de banquise en régime quasi-statique ou transitionnel.

Acknowledgements

I am grateful to Professor Stuart B. Savage for giving me the opportunity to work on this project and for the supervision he has provided throughout my undergraduate and graduate studies. I would also like to thank Olivier Pouliquen and Ricardo Gutfrain for their help and guidance. Benjamin Schonfeld, Fabien Roger and Christian Rojas were very helpful in writing this thesis. This work was supported by an NSERC Strategic Grant titled "Mesoscale Ice Rheology for Regional Ice Forecasting".

à mes parents, Lucille et Gérard

Contents

List of Figures

List of Tables

1 Introduction

There is a great economic demand for ice forecasting at the mesoscale where marine activities, such as navigation, the operation of offshore drilling platforms and commercial fishing, take place. The mesoscale involves time scales of the order of two days and length scales of the order of 100 km. The offshore economic zones of Canada are the Gulf of Saint-Lawrence, the Beaufort Sea and the Labrador Sea. At present, the models being used for ice forecasting are continuum models that are suitable for large length and time scales and they can not, therefore, satisfy the existing economic needs. In order to study ice rheology at the mesoscale, a research program has been initiated. This program involves collaboration between McGill University, the Ice Centre of Environment Canada (AES), and the National Research Council of Canada. A model is being developed in which broken ice fields, due to their discrete nature, are considered to be a two-dimensional granular medium. Thus, the movements and interactions of ice floes are studied by granular dynamics simulations involving floe collisions. The ice floes are considered to move under the action of wind drag, water drag, and the Coriolis force. Normal and tangential contact forces are evaluated at contacts between floes.

The focus of the present work is on the improvement of the model such that it better reflects the interactions between the air, the ice floes, and the water and that the floe collisions be more properly treated. The thesis has two objectives:

· to develop expressions for the wind and water drag such that their non-linear effects are accounted for by the model,

and

· to study the effects of an incrementally slipping tangential force model which involves elastic deformation of the floes in the tangential direction of their contacts.

In the following chapter the effects of the atmosphere and ocean on the motion of ice floes are considered. A general discussion of granular materials and of the numerical methods used to investigate their dynamics, are given in Chapter 3. The details of the discrete element model are presented in this chapter. The expressions for the wind and water drag acting on individual ice floes are developed in Chapter 4. In Chapter 5, the effects of particles shearing are investigated through granular dynamics simulations of a two-dimensional granular material that undergoes a transition from a quasi-static to a rapid flow regime. The behaviour of a broken ice field is analysed, in the same chapter, by simulations performed with the use of the incrementally slipping friction force model. A summary is given and some conclusions are drawn in the last chapter of the thesis.

2 The Effects of the Atmosphere and Ocean on the Motion of Ice Floes

2.1 Equations of motion for a rotating system

Geophysical fluids evolve in a rotating system at an angular velocity Ω of $7.292 \times 10^{-5}s^{-1}$. These fluids are subjected to forces that can be regarded as either fundamental or apparent. The fundamental forces are those corresponding to Newton's second law for motion taking place in a system having coordinates that are fixed in space. These forces are due for instance, to friction, pressure and gravitation. The apparent forces are those associated with a system having a frame of reference rotating with the earth. The Coriolis and centrifugal forces belong to this category.

The equations of motion for the geophysical fluids can be obtained by first considering a fluid element connected to the earth's center through a vector **R**. The absolute time variation of **R** has two components: the velocity of the particle relative to the earth's surface and the velocity of the rotating system at the location of the fluid element, i.e.

$$\frac{d_a\mathbf{R}}{dt} = \frac{d_r\mathbf{R}}{dt} + \mathbf{\Omega} \times \mathbf{R}. \tag{1}$$

The subscripts a and r denote absolute and relative variations respectively. The acceleration is expressed as the variation of the velocity with time such that

$$\frac{d_a\mathbf{V}_a}{dt} = \frac{d_r\mathbf{V}_a}{dt} + \mathbf{\Omega} \times \mathbf{V}_a. \tag{2}$$

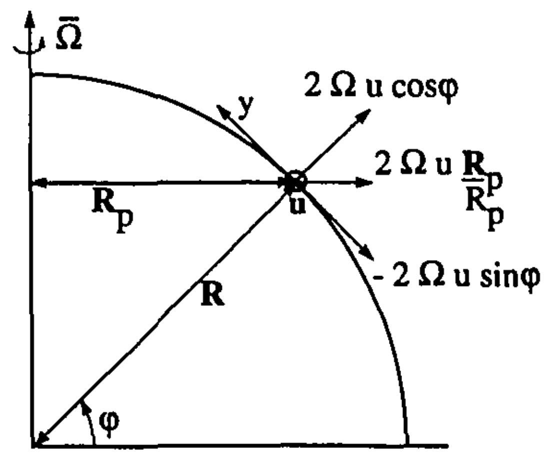

Figure 1: Components of the Coriolis force acting on a fluid element located in the northern hemisphere and moving eastward.

Substituting equation (1) in the previous equation and neglecting the variation with time of $\mathbf{\Omega}$ the absolute acceleration becomes

$$\frac{d_a \mathbf{V}_a}{dt} = \frac{d_r \mathbf{V}_r}{dt} + 2\,\mathbf{\Omega} \times \mathbf{V}_r - \mathbf{\Omega}^2\,\mathbf{R}_p \tag{3}$$

where $2\,\mathbf{\Omega} \times \mathbf{V}$ is the Coriolis acceleration and $\mathbf{\Omega}^2\, R_p{}^2$ is the centripetal acceleration. The component of $\mathbf{R}$ perpendicular to the axis of rotation of the earth is termed $\mathbf{R}_p$ and is illustrated in Figure 1. The Coriolis acceleration, or the Coriolis force per unit mass, acts in a plane perpendicular to $\mathbf{\Omega}$ and to $\mathbf{V}_r$. The Coriolis force can be divided into two components as shown in Figure 1, one acts in the vertical direction and the second one acts at $\pi/2$ from the velocity vector in the horizontal plane. For the northern hemisphere considered in Figure 1 and for a fluid element located at angle φ from the equator and moving in the east direction there will be a component, $-2\Omega u \cos\varphi$, of the force acting towards the sky and a second one,$-2\Omega u \sin\varphi$, pointing south. Since the Coriolis force acts in a direction perpendicular to the fluid element, it can modify the direction of the fluid but not its speed.

The summation of the fundamental forces, $\sum \mathbf{F}$, acting on the fluid element having a density ρ corresponds to $\frac{d_a \mathbf{V}_a}{dt}\rho$ and thus equation (3) can be written as follows

$$\frac{D\mathbf{V}}{Dt} = -2\,\mathbf{\Omega} \times \mathbf{V} + \mathbf{\Omega}^2\,\mathbf{R}_p + \frac{\sum \mathbf{F}}{\rho}. \tag{4}$$

The subscript r has been omitted in the above equation since all the velocity terms involved are relative to the earth, this convention will prevail from now on. The fundamental forces acting on the fluid element are those related to a pressure gradient, to gravitation and to viscosity. To the gravitational force, which is the attraction of the earth on the fluid element, is added the centrifugal force $\Omega^2\mathbf{R}_p$ to create the force known as gravity. The gravity force per unit mass, $\mathbf{g}$, is everywhere normal to the earth's surface and therefore has a direction which slightly deviates from the earth's center except at the equator. Viscous forces are present in all geophysical fluids and result from internal friction between neighboring layers of fluid. They can be expressed as $\nabla\boldsymbol{\tau}/\rho$ where the viscous stresses, $\boldsymbol{\tau}$, for a Newtonian fluid are linearly related to the velocity gradient by the fluid viscosity such that $\boldsymbol{\tau} = \mu\nabla\mathbf{V}$. The viscous forces can therefore be expressed as $\nu\nabla^2\mathbf{V}$, where ν is the kinematic viscosity. The fundamental forces now being clearly defined it is possible to express the equations of motion for the geophysical fluids as follows

$$\frac{D\mathbf{V}}{Dt} = -\frac{1}{\rho}\nabla p - 2\mathbf{\Omega} \times \mathbf{V} + \mathbf{g} + \nu\nabla^2\mathbf{V}. \qquad (5)$$

The friction forces just calculated are for laminar flows. The viscous effects are of significance in relatively small layers at the earth's surface or at the water surface where vertical shear is important. For the usual cases where turbulence is predominant the stresses will correspond to the momentum fluxes due to turbulent motion. These turbulent or Reynold's stresses are associated with the velocity fluctuations and are approximated using an eddy viscosity coefficient, which is a property of the flow rather than a property of the fluid.

2.2 The geostrophic approximation

In meteorology and in oceanography the various phenomena observed such as tides and cyclones are studied according to a scale analysis. This technique consists of evaluating the different terms of equation (5) and estimating the order of magnitude of the variables as well as the amplitude of their fluctuations and the characteristic dimensions of their fluctuations. The comparison of the different terms will permit us to eliminate the weakest ones and thus to simplify the solution of the equations of motion. There are five distinct scales: planetary, synoptic, mesoscale, local, and finally the microscale. The following are some examples of the phenomena associated with these scales: tides are studied at the planetary scale, cyclones at the synoptic scale, fronts at the mesoscale, convection at the local scale and waves at the microscale.

The purpose of this section is to introduce the geostrophic approximation and for that we need to know more about the synoptic scale. The length of this scale is 10^6

metres for the atmosphere and 10^5 metres for the ocean; its time scale is of the order of a few days for both environments. At the synoptic scale the horizontal components of the pressure gradient and of the Coriolis force are of the same order of magnitude and nearly balance each other. The other terms of equation (5) are at least one order of magnitude smaller and can be neglected in the analysis of the synoptic scale. Conserving only the Coriolis and the pressure gradient terms from equation (5) we obtain the geostrophic approximation

$$-f\,v_g = -\frac{1}{\rho}\frac{\partial p}{\partial x}, \tag{6}$$

$$f\,u_g = -\frac{1}{\rho}\frac{\partial p}{\partial y}, \tag{7}$$

where f is the Coriolis parameter corresponding to $2\Omega\sin\varphi$, and u_g and v_g are the respective x and y components of the geostrophic velocity. The expression for the geostrophic velocity vector can thus be written as follows

$$\mathbf{V}_g = \mathbf{k} \times \frac{1}{\rho f}\nabla p, \tag{8}$$

where $\mathbf{k}$ is a unit vector in the vertical direction. The establishment of the geostrophic winds can be visualized by looking at a parcel of air moving from an area of high pressure to one of low pressure (Figure 2). The fluid particle is first subjected to a pressure force perpendicular to the isobars that will cause the particle to rise. Once the movement is initiated the Coriolis force, which is perpendicular to the fluid's velocity, tends to deviate the fluid's trajectory to the right. As the velocity of the fluid

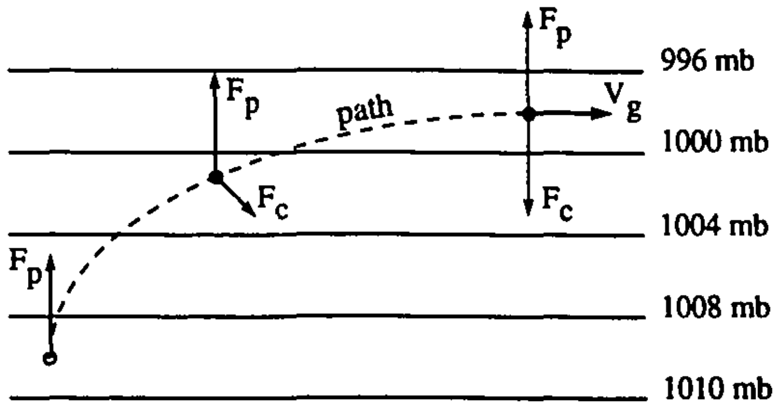

Figure 2: The establishment of the geostrophic wind (northern hemisphere); F_p is the pressure-gradient force, and F_c the Coriolis force.

element increases the Coriolis force increases proportionally. The particle's direction will be modified until it becomes parallel to the isobars, at this point the Coriolis force associated with the velocity of the particle will balance the pressure gradient force.

2.3 Pure wind-drift currents and the Ekman spiral

Wind drift is a force of major importance for the upper ocean. Water currents are principally caused by the presence of a horizontal pressure gradient resulting from sea surface tilt, and by the action of the wind blowing on the sea surface. If we consider the ocean as being divided into a series of thin layers where on the topmost layer a wind stress τ is applied, then this layer will exert a shear stress $\tau - d\tau$ on the underlying layer. This second layer will itself exert a frictional stress on the third layer that will be decreased by $d\tau$. Thus, for a fluid element of the first layer and of mass $\rho\, dz\, dx\, dy$

the net frictional force acting on it is

$$dx\, dy\, (\tau - (\tau - \frac{\partial \tau}{\partial z} dz)) \;=\; \frac{\partial \tau}{\partial z}\, dx\, dy\, dz$$

and this force per unit mass is $\frac{\partial \tau}{\partial z}/\rho$. The motion of a volume element of fluid is determined by the frictional forces, the Coriolis force and by the pressure gradients acting on it and therefore will follow these equations

$$\frac{du}{dt} - fv = -\frac{1}{\rho}\frac{\partial p}{\partial x} + \frac{1}{\rho}\frac{\partial \tau_x}{\partial z}, \tag{9}$$

$$\frac{dv}{dt} + fu = -\frac{1}{\rho}\frac{\partial p}{\partial y} + \frac{1}{\rho}\frac{\partial \tau_y}{\partial z}. \tag{10}$$

Writing the above equations for a laminar steady flow and for a Newtonian fluid we obtain

$$- fv = -\frac{1}{\rho}\frac{\partial p}{\partial x} + \nu\frac{\partial^2 u}{\partial z^2}, \tag{11}$$

$$fu = -\frac{1}{\rho}\frac{\partial p}{\partial y} + \nu\frac{\partial^2 v}{\partial z^2}. \tag{12}$$

As mentioned previously the Coriolis force can only modify the direction of the fluid element and thus, only the two remaining forces tend to accelerate the fluid. The effects of sea surface tilt and of wind drift can be considered separately such that the velocity will have two components, one due to pressure and the other due to friction. The component of the velocity uniquely related to the pressure gradient is the geostrophic current. The second component associated with the wind stress is the Ekman velocity

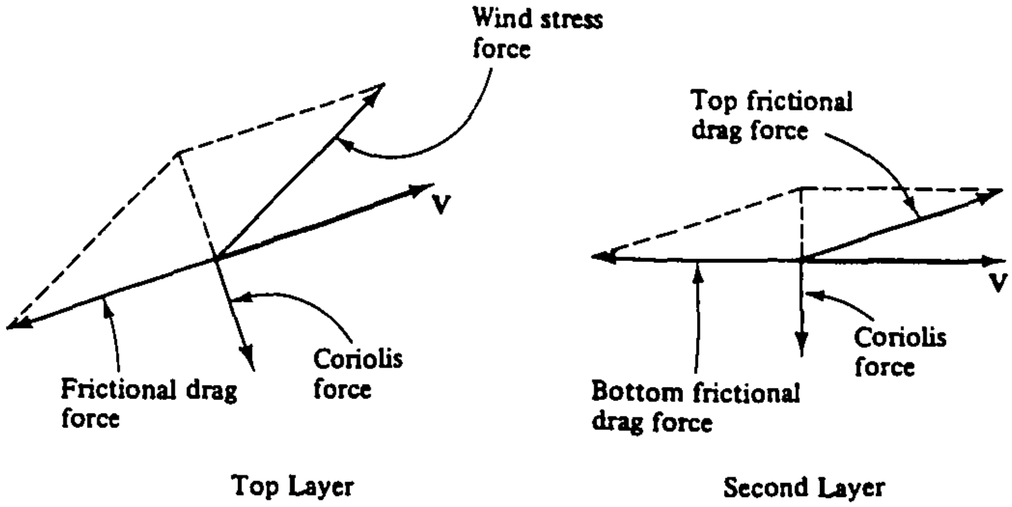

Figure 3: Balance of forces acting on fluid element for Ekman wind-drift currents [von Schmind, 1980].

derived by Ekman [1905] who considered the nonaccelerated pure wind drift currents for an ocean infinitely deep and unbounded in the horizontal. For pure wind-drift currents the equations of motion can be written in terms of total derivatives and are simply the following

$$-fv_E = \nu \frac{d^2 u_E}{dz^2}, \tag{13}$$

$$fu_E = \nu \frac{d^2 v_E}{dz^2}, \tag{14}$$

where the subscript E stands for Ekman. The balance of the forces acting on the two topmost layers is illustrated in Figure 3. As shown in this figure the resisting force for the first layer becomes the driving force for the second layer. Solutions for u_E and v_E can be obtained by first differentiating equation (13) twice and then substituting the expression for d^2v_E/dz^2 in (14) such that the following equation is obtained

$$\frac{d^4u_E}{dz^4} + (\frac{f}{\nu})^2 u_E = 0, \tag{15}$$

which has the following general solution

$$u_E = B_1 e^{(1+i)z/\delta_E} + B_2 e^{-(1+i)z/\delta_E} + B_3 e^{(1-i)z/\delta_E} + B_4 e^{-(1-i)z/\delta_E} \tag{16}$$

where δ_E is defined as $\sqrt{2\nu/f}$. In order to evaluate the constants B_1, B_2, B_3 and B_4 the boundary conditions have to be stated. First, it is assumed that the wind blows in the x direction and that according to Newton's law of viscosity the stress is given by

$$\tau = \mu \frac{du_E}{dz}\Big|_{z=0} \tag{17}$$

and consequently

$$0 = \mu \frac{dv_E}{dz}\Big|_{z=0} . \tag{18}$$

At great depths the wind drift currents disappear such that

$$u_E \Big|_{z=-\infty} = 0 \tag{19}$$

and

$$v_E \Big|_{z=-\infty} = 0. \tag{20}$$

At this point it is possible to obtain the expressions for u_E and v_E as functions of the depth z

$$u_E = \frac{\tau\,\delta_E}{\sqrt{2}\mu}\, e^{z/\delta_E} \sin\left(\frac{z}{\delta_E} + \frac{\pi}{4}\right), \tag{21}$$

$$v_E = -\frac{\tau\,\delta_E}{\sqrt{2}\mu}\, e^{z/\delta_E} \cos\left(\frac{z}{\delta_E} + \frac{\pi}{4}\right). \tag{22}$$

At the water surface where $z = 0$ the velocity components are

$$u_E\,|_{z=0} = \frac{\tau\,\delta_E}{\sqrt{2}\mu}\sin(\frac{\pi}{4}), \tag{23}$$

$$v_E\,|_{z=0} = -\frac{\tau\,\delta_E}{\sqrt{2}\mu}\cos(\frac{\pi}{4}). \tag{24}$$

The surface velocity vector $\mathbf{V}_o$ has a magnitude of $\tau\,\delta_E/\sqrt{2}\,\mu$. Therefore, the water velocity at the surface is

$$\mathbf{V}_o = \frac{\sqrt{2}}{2}V_o\,\mathbf{i} - \frac{\sqrt{2}}{2}V_o\,\mathbf{j}. \tag{25}$$

This vector points in a direction 45° to the right of the wind direction in the Northern Hemisphere for which this solution was obtained. For the case of Southern Hemisphere the water current is directed 45° to the left of the wind stress. The magnitude of the velocity vector decreases exponentially with depth and its direction is modified such that it gradually turns clockwise. When the velocity vectors for several depths are sketched on the same plane, a spiral is formed as shown in Figure 4; it is known as

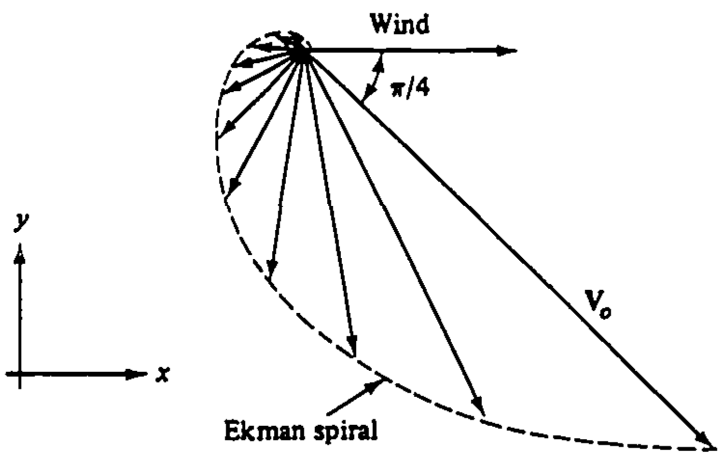

Figure 4: Ekman spiral for wind drift in the northern hemisphere [von Schmind, 1980].

the Ekman spiral. Ekman defined the depth at which the frictional forces produced by the wind become negligible as the 'depth of frictional resistance'. At this depth, corresponding to $-\pi\ell_E$, the water current is in a direction opposite to the surface current.

The mass transports in the x and y directions are found by integrating, in the z direction, the corresponding velocity components multiplied by the fluid density. The following mass transports are obtained from the integrations

$$M_x = 0, \tag{26}$$

$$M_y = -\frac{\tau H^2}{2\nu}. \tag{27}$$

The total mass transport is in the negative y direction or in other words is directed 90° *cum sole* to the wind direction. The flux transverse to the isobars in the Ekman layer is a mechanism of dissipation of kinetic energy and therefore the preceding theory, appropriate for the laminar case, is not applicable quantitatively to the real environments but still provides a good idea of the processes that take place in the upper ocean.

2.4 The oceanic boundary layer and the balance of forces for ice floes

In northern regions the ocean is covered with ice. In some areas, like the Labrador sea or in the marginal ice zone of the Arctic, the ice cover is fractured, forming floes having sizes that can range from a few meters to several kilometers. The characteristics of the ice floes vary with the seasons. During the summer, for example, they become smaller and the ice is less resistant. The motion of the ice floes is primarily dictated by the action of the wind. The momentum induced by the wind is transported downward by the ice cover to the water and to the planetary boundary layer such that the shear stress acting at the ice-water interface generally resists the motion of the ice floes. Moreover the ice floes are subjected to a Coriolis force which is significant at high latitudes, to a pressure gradient force resulting from sea surface tilt and also to contact forces due to internal collisions.

A study having a major impact in the field of ice dynamics was conducted in the early seventies in the Arctic ocean. It was called *Arctic Ice Dynamics Joint Experiment* (AIDJEX). The purpose of AIDJEX was to "understand quantitatively the interaction between the fields of motion of the atmosphere, the pack ice, and the ocean". In the 1972 pilot study of AIDJEX an investigation, consisting of taking velocity measurements for the ice, the wind and the water currents, was done at several stations. The water currents were measured at several depths underneath the ice floes, on which the stations were located, down to 50 meters. These field data were used by Hunkins [1974] in order to find the balance of forces for several ice floes, and that for different time intervals. Water stresses were calculated based on the momentum exchange in the surface boundary layer. The other external forces, consisting of wind drag, Coriolis force and pressure gradients, were calculated based on the velocity measurements of the ice and wind.

The momentum integral method used by Hunkins [1974] to evaluate the water stresses will now be briefly presented and it will be followed by the details of the computations of the other forces. The water velocities recorded in the field study were averaged over twelve hours in order to minimize the fluctuations related to turbulence and to inertial oscillations. Hodographs of the current velocities measured at several depths between 0 and 50 meters are presented in Figure 5. On the hodographs are given the two velocity components of the water currents for several depths. Beside each point is written the corresponding depth and these points are connected by lines on the graphs. The 0 depth corresponds to the base of the ice which is 2 m below sea level. The dashed line on the hodographs corresponds to the surface boundary layer in which the frictional forces are more significant than the Coriolis effects. Below 2 m is the Ekman layer where changes in the current's direction and speed are significant. The spirals obtained on the hodographs do not correspond exactly to the theoretical Ekman spiral since the velocity decreases sporadically and the rotation of the current is merely gradual. Underneath the Ekman layer the frictional effects are non-existent and the current is quasi-geostrophic. From the hodographs obtained in his study, Hunkins [1974] determined that the geostrophic current was between 25 and 50 m from the

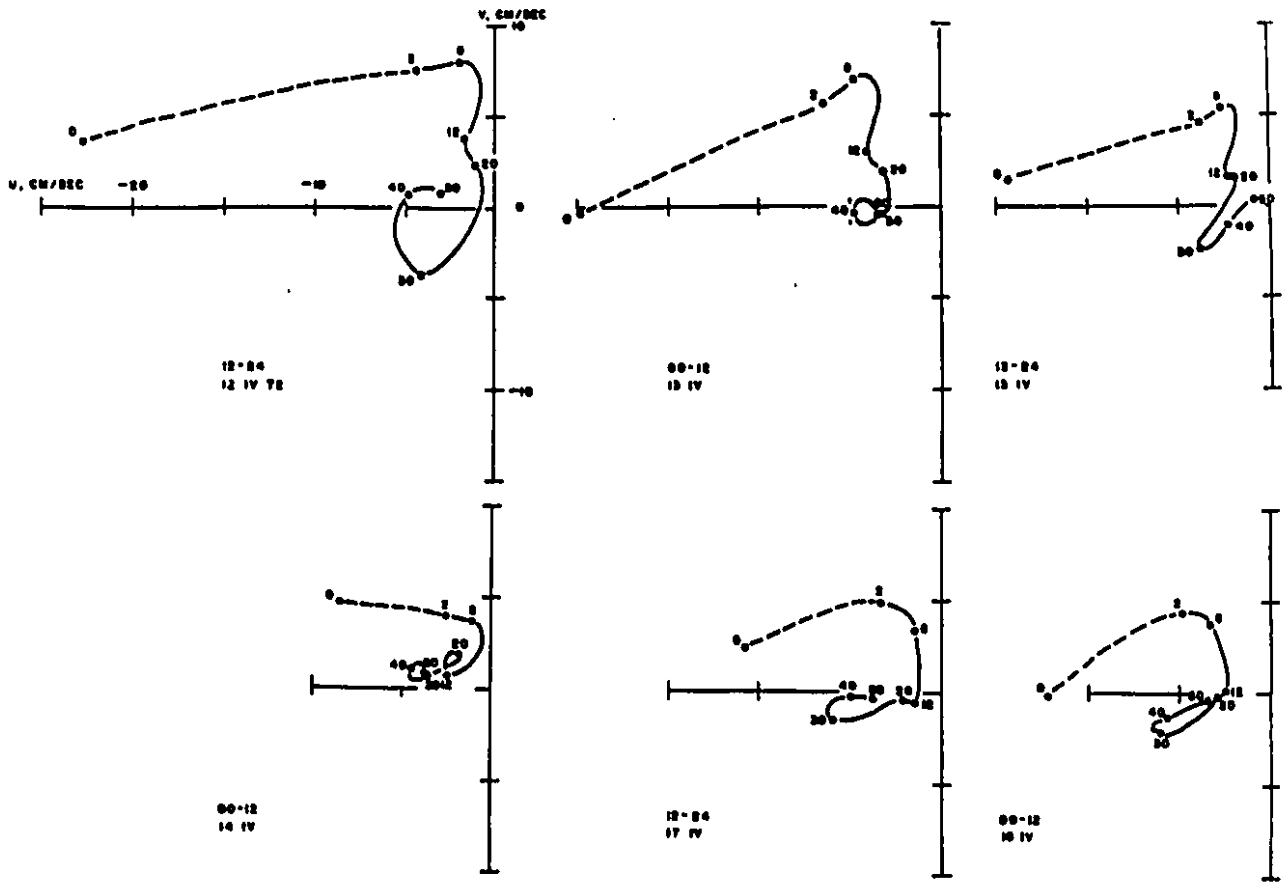

Figure 5: Hodographs of absolute currents for 12-hour intervals with ice drift greater than 9 m/s. Depths in meters below ice base. North at top of page. Local standard time [Hunkins, 1974].

surface.

The x (east) and y (north) components of the ice-water stress, τ_o, were evaluated using the vertically integrated form of the equations of motion

$$\frac{\partial M_x}{\partial t} - fM_y = \tau_{ox}, \tag{28}$$

$$\frac{\partial M_y}{\partial t} + fM_y = \tau_{oy}, \tag{29}$$

where f is the Coriolis parameter described in §2.2 and M_x and M_y are the mass transports given by

$$M_x = \int_{H_E}^{0} \rho_w (u - u_g) dz, \tag{30}$$

$$M_y = \int_{H_E}^{0} \rho_w (v - v_g) dz, \tag{31}$$

where H_E is the depth of frictional influence chosen to be 25 m. The geostrophic velocity components, u_g and v_g, were evaluated at this depth and were considered to be constant throughout the Ekman layer. The water density, ρ_w, was taken to be 1.0 g/cm^3. The time dependent terms were evaluated by taking the hourly differences between mass transports.

The air shear stresses were determined through the following drag law

$$\boldsymbol{\tau}_a = \rho_a C_a \mathbf{V}_{10}{}^2 \tag{32}$$

where C_a is the air drag coefficient taken to be 1.5×10^{-3}, ρ_a is the air density of

0.00125 g/cm^3 and V_{10} is the 10-m surface wind velocity. The Coriolis force for an ice floe having a thickness h of 2.5 m , a density ρ_i of 0.9 g/cm^3, and being located at a latitude of 75° was evaluated using the following relationships

$$F_{cx} = \rho_i h f v_i, \tag{33}$$

$$F_{cy} = -\rho_i h f u_i, \tag{34}$$

where u_i and v_i are the two respective x and y components of the ice velocity. The pressure forces were computed using the geostrophic velocity components as follows

$$F_{px} = -\rho_i h f v_g, \tag{35}$$

$$F_{py} = \rho_i h f u_g. \tag{36}$$

The ice was assumed to drift under balanced forces such that the internal ice force due to floe collisions was evaluated as the residual from the force diagram. In Figure 6 are sketched the force vectors acting on four ice floes as well as their velocity vectors. As shown in this figure the internal forces play quite an important role in ice motion. The wind and water stresses were found to point generally in opposite directions and to have a strong correlation in their magnitude as shown in Figure 7 where the two stresses averaged over 12 hours are plotted versus time for a one month period for AIDJEX's main camp. The Coriolis force, the water and wind drag forces are found to be of the same magnitude while the pressure gradient force is less significant.

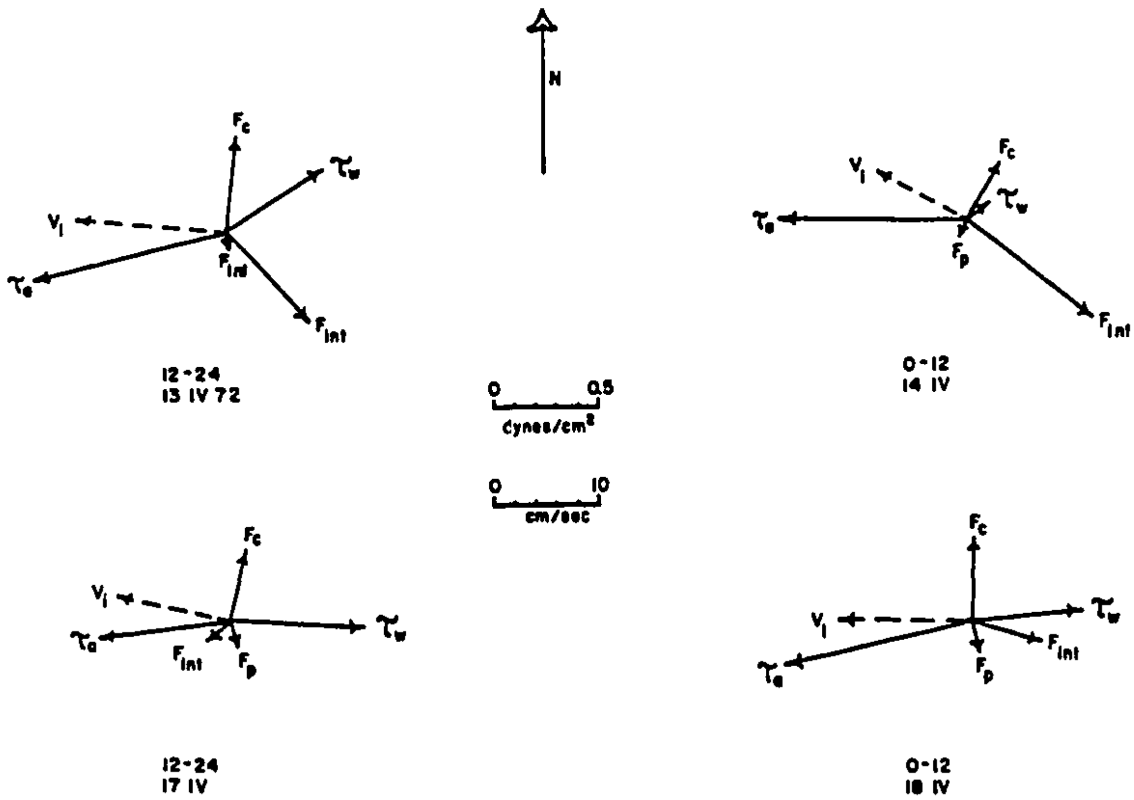

Figure 6: Balance of forces on ice for 12-hour intervals when winds exceeded 5 cm/s. Ice velocity, v_i, in cm/s; air-ice stress, τ_a; ice-water stress, τ_w; Coriolis force, F_c; pressure-gradient force F_p; and internal ice force F_{int}[Hunkins, 1974].

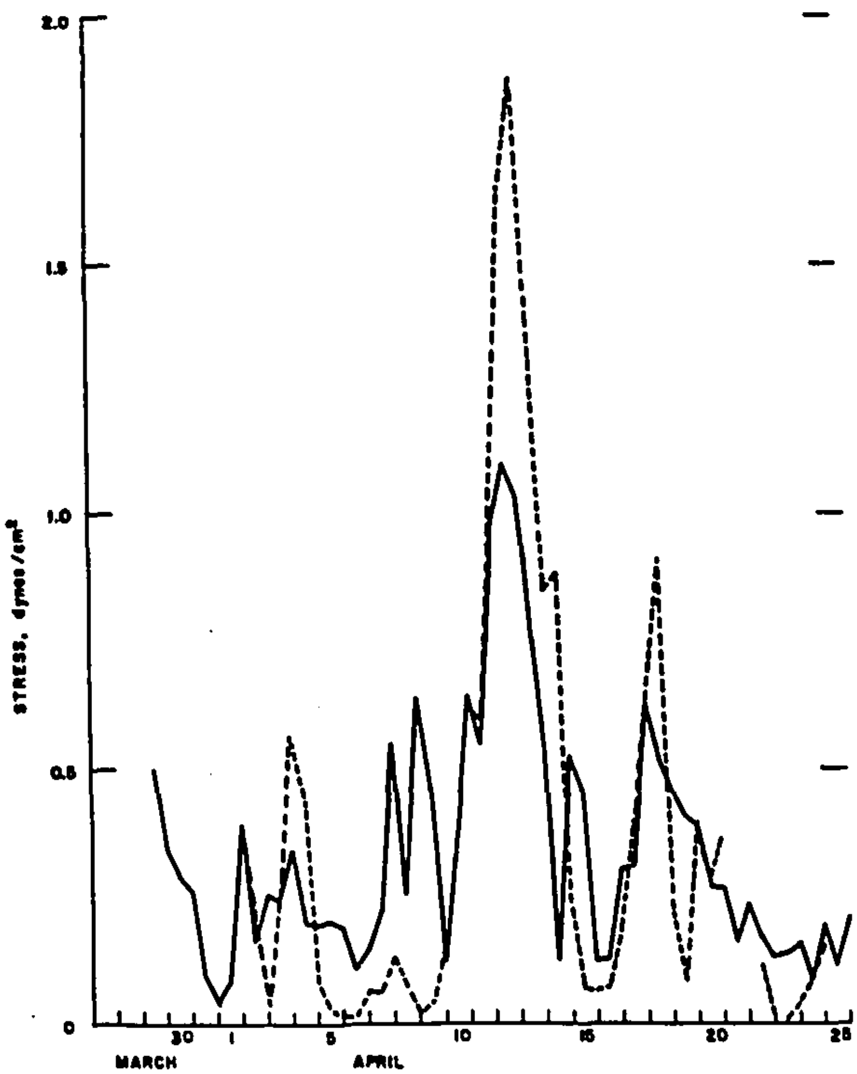

Figure 7: Ice-water (solid line) and air-ice (dashed line) stress at 1972 AIDJEX main camp based on 12-hour means. Direction of air-ice stress reversed for comparison [Hunkins, 1974].

2.4.1 Evaluation of water stresses in sea ice models

The water drag force vector acting on an ice floe is colinear with the ice velocity vector relative to the water current. In oceanographic studies, the geostrophic currents are more easily evaluated than those at the surface. It is therefore important to be able to determine the angle formed by the water stress vector and the relative velocity vector between the ice and the geostrophic current. This angle β, as shown in Figure 8, is referred to as the boundary layer turning angle or simply as the water turning angle. McPhee [1980] has used field data of the AIDJEX study of 1975 to determine the water turning angle as well as a simple expression for the water shear stress. The data used were for the melt season during which the fragmented ice pack is not able to support as much stress as in the winter. McPhee [1980] has demonstrated that for several weeks in 1975 the ice was free of internal forces. This period of *free drift* was identified by considering inertial oscillations, ice-wind currents statistics and simulations of ice drift for the AIDJEX stations. During such a period, the wind stress is balanced by the Coriolis force and by the water stress. The balance of forces is shown in Figure 8. As sketched on this figure the water stress lies at an angle β counterclockwise from the line of action of the relative velocity vector **V** between the ice and the geostrophic current. For a 20-day period at the height of the melt season, ice velocity measurements were made at the four camp stations twice daily. The wind was measured at a height of 10 m and realistic estimates of the mass of the ice floes, of the wind drag coefficient and of the geostrophic currents were made. The water stresses were evaluated from the force balance for cases where the relative ice speed was greater than 8 cm/s; 95 points were determined and plotted on a scatter diagram shown in Figure 9. From a least-squares

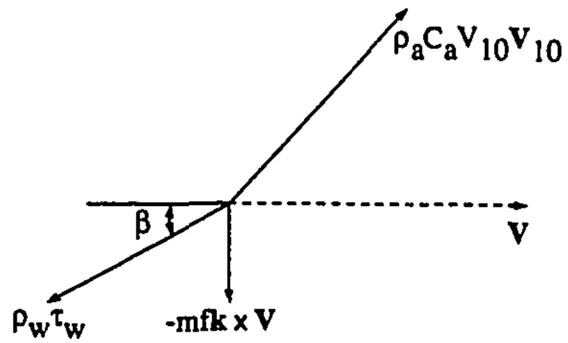

Figure 8: Schematic of the free-drift force balance.

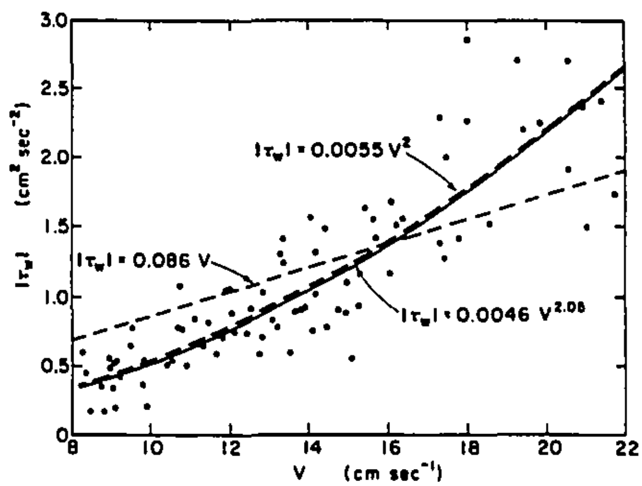

Figure 9: Kinematic water stress versus relative ice speed [McPhee, 1980].

exponential fit the following relationship for the water stress was found

$$|\tau_w| = 0.0046\, V^{2.05}. \tag{37}$$

From this result it appears reasonable to evaluate the water stresses through a quadratic relationship as shown in the graph. The drag coefficient found by a fit of a quadratic expression is 0.0055. This drag coefficient is high, as expected, since the bottom of the ice was observed to be rough. A drag coefficient of 0.0034 was evaluated at one of the AIDJEX camps during the year of 1972 where the ice was considerably smoother [McPhee and Smith, 1976]. The drag coefficient evaluated from the relative velocity between the ice and the geostrophic current is usually called the *geostrophic* drag coefficient. The value of the drag coefficient is related to the under ice surface roughness and to the depth at which current measurements are made.

From the balance of forces obtained in the free drift period, the boundary layer turning angle β was evaluated to be 23.6° on average. For the 1972 pilot study of the AIDJEX camp, a mean value of 24° was found [McPhee and Smith ,1976]. The water stress is to be determined from idealized boundary layers assuming a constant turning angle as follows [Hibler, 1981]

$$\tau_w = C_w{}'[\mathbf{V}\ \cos\beta + \mathbf{k} \times \mathbf{V}\ \sin\beta] \tag{38}$$

where $C_w{}'$ is a constant having units of $\mathrm{kg\,m^{-2}\,s^{-1}}$ in a linear drag law, or it corresponds to

$$C_w' = \rho_w C_w |\mathbf{V}| \tag{39}$$

when the stresses are evaluated using a quadratic relationship. In the above equations ρ_w is the water density and C_w is the dimensionless drag coefficient. As mentioned previously, the drag coefficient and the turning angle vary according to the depth at which the water currents are measured.

2.4.2 Surface winds and air stresses

In section 1.2 we have seen that at the synoptic scale the pressure gradient force and the Coriolis force nearly balance each other and that under such an equilibrium the wind blows parallel to the isobars. In the 500 m or so above the earth's surface, frictional forces are important due to the significant roughness present at the surface of the earth. At the standard anemometer height of 10 m, a force balance is reached for the wind blowing at a counterclockwise angle α to the isobars as illustrated in Figure 10. This angle is analogous to the water turning angle. The magnitude of the friction force and of α is proportional to the wind speed and strongly depends on the roughness of the surface over which the wind blows. The component of the friction force along the isobars is balanced by the corresponding component of the Coriolis force such that the more significant the friction force is, the greater the cross-isobars angle must be. The winds at 10 m above the ocean correspond to about two thirds of their geostrophic speed whereas this ratio is reduced by up to one third for winds blowing over the ground. The air turning angle α is usually between 10° and 20° for water surfaces

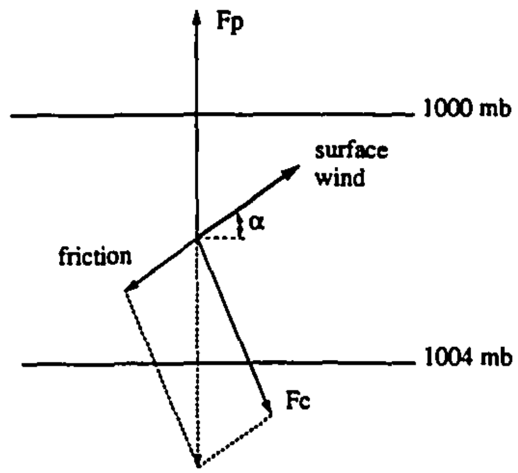

Figure 10: Balance of forces in a surface wind (northern hemisphere).

and 40° or more for ground surfaces. The friction forces diminish slowly with height, consequently the wind speed increases correspondingly and the turning angle gradually decreases. The atmospheric layer where the frictional forces are present is called, as in the ocean, the Ekman layer.

The presence of ice on the water surface considerably increases the surface friction and mean values for α were found, from various studies, to vary from 22° to 42° and their reduction factors of surface to geostrophic winds, V_{10}/V_G, were found to be 0.5 to 0.8. Fissel and Tang [1991] have conducted a study for the Newfoundland Shelf and have found turning angles of 20° for near shore locations, of 35° in the pack ice interior and of 42° near the ice edge. The seasonal variations of α were observed during AIDJEX by Carsey [1980]. For the spring a minimum mean turning angle of 19.2° was found versus a maximum of 31.4° for the fall. According to Fissel and Tang [1991] the considerably higher values obtained for the turning angles in the Newfoundland shelf are related to to the very high roughness of the ice cover and to the small floe sizes.

Overland [1985] has done a literature review of ice-atmosphere interaction studies and reports that the air drag is greater over storm-broken ice.

The drag exerted by the wind on the ice is related to the relative velocity between the wind and the ice, but the wind stress can be accurately evaluated by neglecting the ice velocity since it represents only a few percent of the wind velocity. The wind stress, assuming a constant turning angle, is determined as follows [Hibler, 1981]

$$\tau_a = C_a{}'[\mathbf{V}_a \cos\alpha + \mathbf{k} \times \mathbf{V}_a \sin\alpha] \tag{40}$$

where $C_a{}'$ is defined differently depending wether a linear or a quadratic drag law is used. In a linear drag law $C_a{}'$ is a constant, having units of $\mathrm{kg\,m^{-2}\,s^{-1}}$. When the stresses are estimated by a quadratic relationship $C_a{}'$ corresponds to

$$C_a{}' = \rho_a\, C_a\, |\mathbf{V}_a| \tag{41}$$

where C_a is a dimensionless drag coefficient and ρ_a is the air density. In the two previous equations, $\mathbf{V}_a$ is the wind velocity corresponding to the geostrophic wind evaluated from barometric maps. If the 10-m surface wind is used in equation (40) and (41) α is zero due to the fact that the wind stress is colinear with the wind's velocity vector.

2.5 References

Carsey, F.D. 1980. The boundary layer height in air stress measurement. *Sea Ice Processes and Models*, edited by R.S. Pritchard, University of Washington Press, Seattle and London, 443-451.

Ekman, V.W. 1905. On the influence of earth's rotation on ocean current. *Ark. Mat. Astr. Sys.*, vol. 2, 1-52.

Fissel, D.B. and Tang, C.L. 1991. Response of sea ice drift to wind forcing on the Northeastern Newfoundland shelf. *J. Geophys. Res.*, **96**, 18,397-18,409.

Flato, G.M. and Hibler, W.D. 1989. The effect of ice pressure on marginal ice zone dynamics. *IEEE Trans. on Geoscience and Remote Sensing*, **27**, 514-521.

Hibler, W.D. 1981. Ice dynamics. *The Geophysics of Sea Ice*, edited by Norbert Untersteiner, Plenum Press, New York and London, 577-640.

Hunkins, K. 1974. The oceanic boundary layer and ice-water stress during AIDJEX 1972. *AIDJEX Bulletin*, **26**, 109-122.

Mcphee, M.G. 1980. An analysis of pack ice drift in summer. *Sea Ice Processes and Models*, edited by R.S. Pritchard, University of Washington Press, Seattle, 62-75.

McPhee, M.G. and Smith, J.D. 1976. Measurement of the turbulent boundary layer under pack ice. *J. Phys. Oceanogr.*, **6**, 696-711.

Overland, J.E. 1985. Atmospheric boundary layer structure and drag coefficients over sea ice. *J. Geophys. Res.*, **90**, 9029-9049.

von Schmind, J.J. 1980. *Geophysical Fluid Dynamics for Oceanographers.* Prentice-Hall, Inc., Englewoood Cliffs, N.J.

3 Granular Dynamics Simulations Procedures

This chapter describes the discrete element model that is being used to investigate the dynamics of the marginal ice zone. The fractured ice cover is considered to be a two dimensional granular medium and the simulations are done according to a molecular dynamics approach which is commonly used to study granular flows. Before presenting the details of the numerical procedure involved in the ice floe problem, some physical aspects of granular materials and of their flows will be discussed and then followed by an overview of the granular dynamics type of computations.

3.1 What is a granular material ?

Matter is encountered in a granular form in nature as well as in industry. A granular material consists of a large number of solid particles whose interstices are filled by a fluid. The fluid in which the solid particles are dispersed can be air when we think of powders for example, or a liquid when slurries, pastes or suspensions are involved. The following are some examples of granular media: food stuff such as cereals, sugar or flour, animal feed, sand, granular snow, metal and ceramic powders. What is very particular about granular material is that sometimes it behaves like a solid and at other times like a liquid. Consider, as an example of this phenomenon, the pile of mustard grains shown in Figure 11 A. This pile is stable and in static equilibrium when its slope is less than a certain value called the angle of repose. Past this value the grains that will be added to the pile will flow on the sides forming an avalanche. It is possible to see a thin layer of the grains flowing at the surface of the pile as in Figure 11 B. One can consider the static pile as behaving like a solid, whereas a liquid-like behaviour is associated with the avalanche.

A parameter describing the internal behaviour of a pile is the internal friction angle of the material, Φ, which is closely related to the angle of repose. The internal friction angle is defined by the Mohr Coulomb yield criterion. This theory states that failure will occur on a plane when the shear stress acting on this plane becomes equal to the product of the normal stress σ with the tangent of the friction angle, Φ, such that

$$|\tau| = \sigma \tan \Phi. \tag{42}$$

The internal friction angle depends on the geometry of the particles and also on their roughness. The more angular the particles are, the greater Φ is.

Another very interesting characteristic of a granular material is its capacity of forming arches such that only a small fraction of the material can sustain most of the weight of a pile. In a cereal box, for example, the grains on the sides are sustained by friction and these forces are transmitted to the other grains by inter-particle contacts developing a force network. Under these conditions the grains at the bottom of the box are not being crushed since there is barely any weight resting on them. Some experiments have been performed involving plexiglass cylinders that were submitted to a vertical pressure. Plexiglass has the property of being optically anisotropic such that when the cylinders were subjected to a polarized light it was possible to observe the force network developed between particles. A picture of the cylinders' pile is shown in Figure 12 and the brightest cylinders are those transmitting the vertical constraint. As expected, only a small fraction of the cylinders are supporting the weight. The

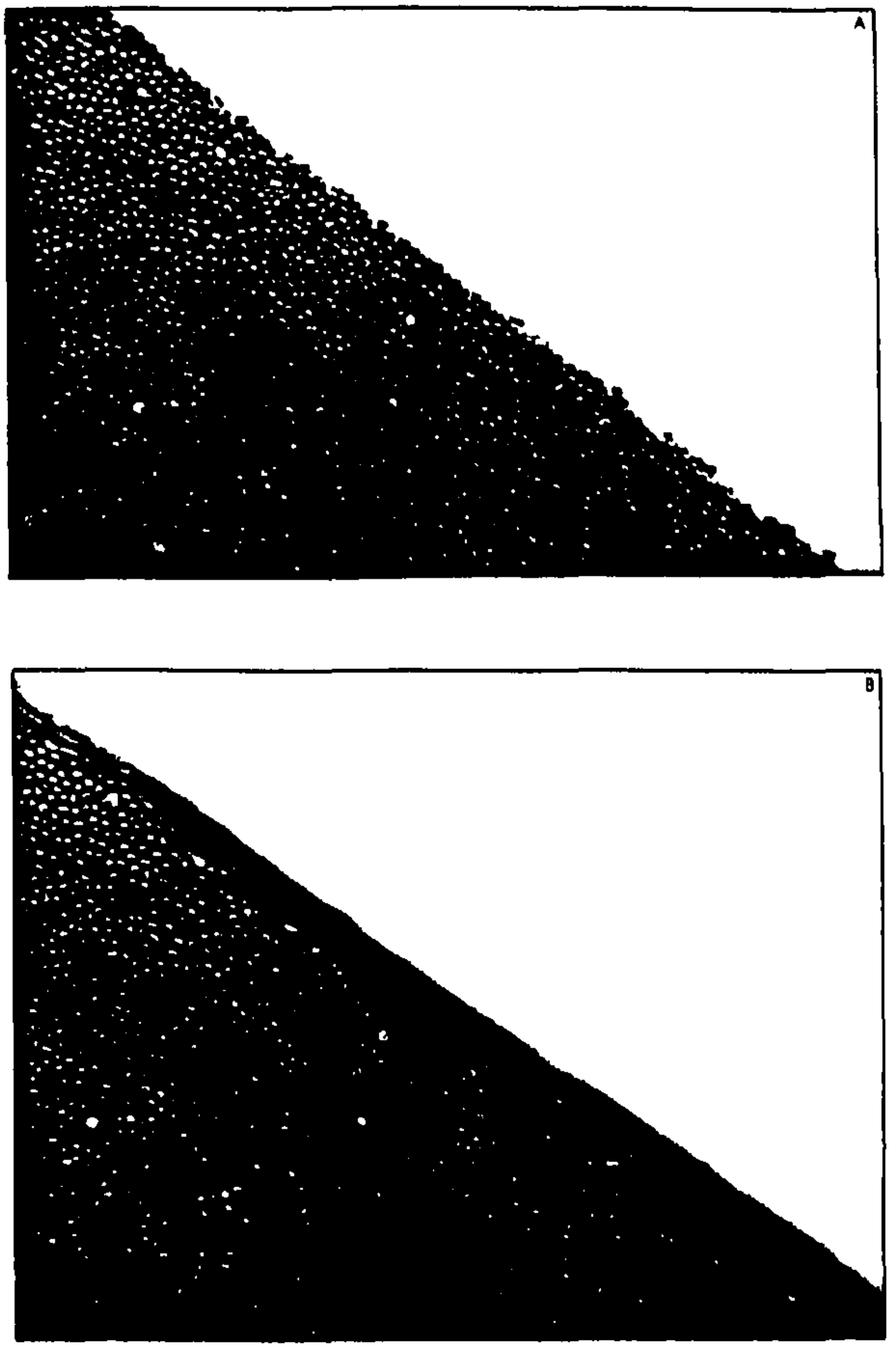

Figure 11: A. Mustard grain pile in static equilibrium. B. Avalanche of a thin layer at the top of the pile [Jaeger and Nagel, 1992].

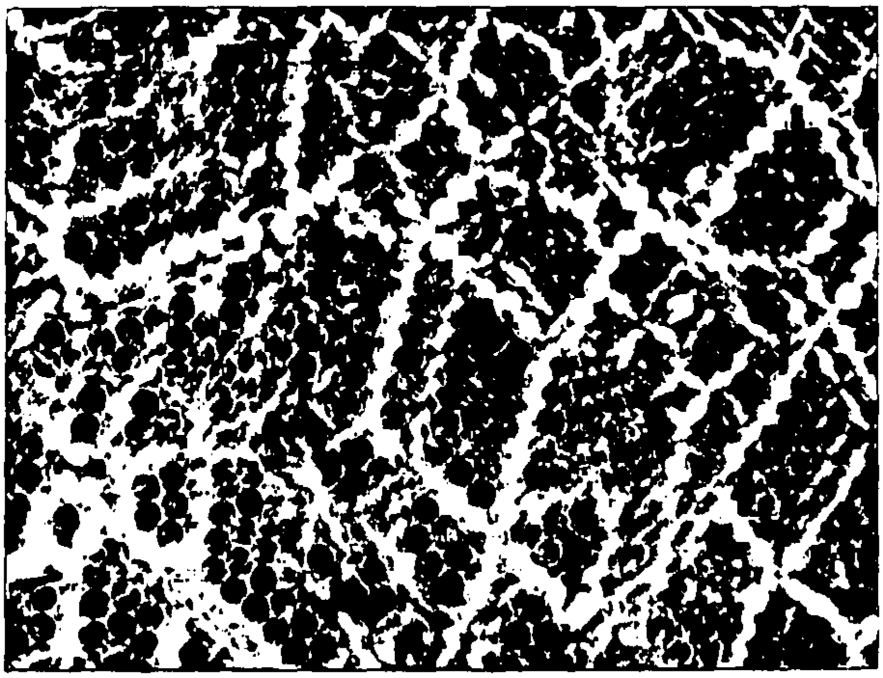

Figure 12: Plexiglass cylinders subjected to a vertical pressure. The lightened cylinders are those transmitting the constraint [Jaeger and Nagel, 1992].

capacity of the particles to make arches is present in most high concentration granular flow regimes.

3.2 Granular Flows

Flows of granular material take place in many environments and under various conditions. Some examples are

- sediment transports in rivers,
- manipulation of pharmaceutical products in industry,
- snow avalanches,
- the mixing of aggregates utilized in the making of asphalt or concrete in a rotating cylinder,
- land slides

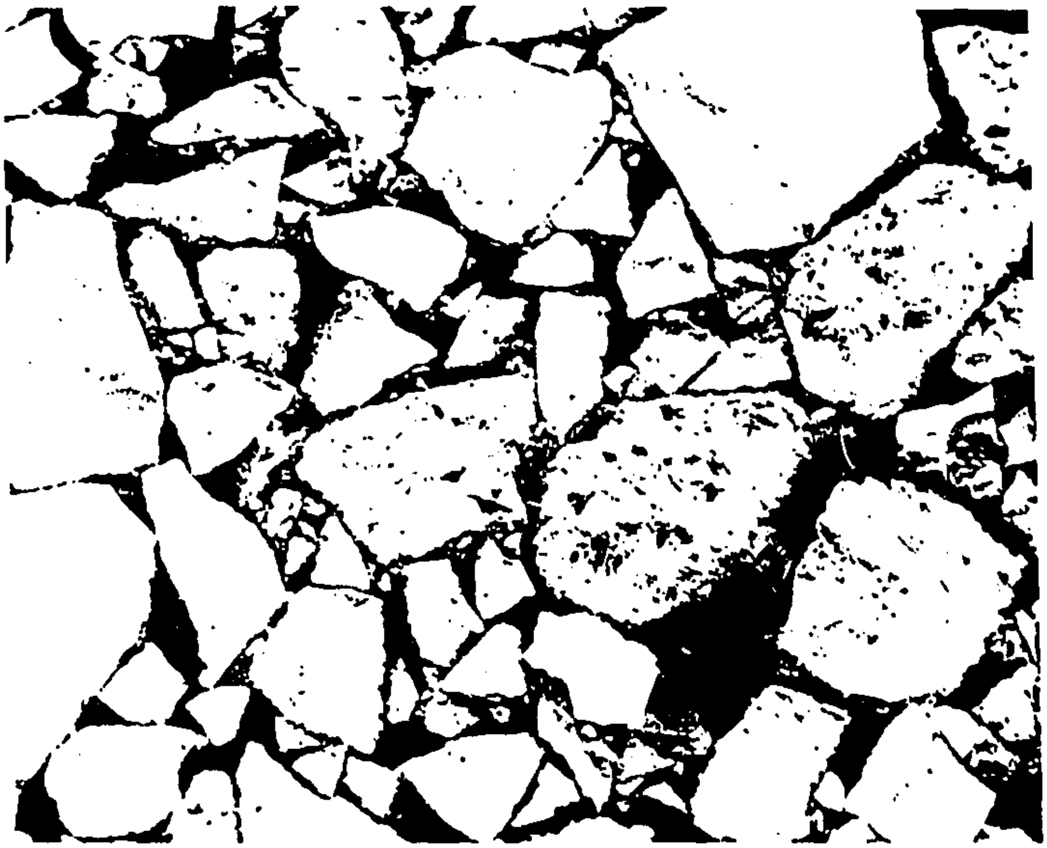

Figure 13: Photograph of ice floes taken in the marginal ice zone of the East Greenland Sea. The largest floes have diameters of approximately 50 m [Leppäranta and Hibler, 1987].

and the subject of the present study;

· the movements of ice floes forming a broken ice field.

From field observations made in the East Greenland marginal ice zone, Leppäranta and Hibler [1987] noticed that "... the ice pack could be considered an almost ideal two-dimensional granular medium". A picture of the ice floes covering a surface of approximately 0.7 km^2 was taken from their paper and is presented in Figure 13.

3.2.1 Granular flow regimes

Bagnold [1954] has classified granular flows in three distinct regimes:

· a macro-viscous regime for granular flows in which the normal and shear stresses are proportional to the velocity gradient and in which the viscosity is dominant,

· a grain-inertia regime where the particles' interactions control the flow behaviour as opposed to the interstitial fluid effects that are negligible in their flow regime,

·and an intermediate regime that Bagnold called transitional.

In the grain-inertia regime Bagnold was able to find an expression for the stresses where they depend on the square of the velocity gradient. Such a relationship between the stresses and the velocity gradient was developed by expressing the particles' motion in terms of the mean velocities and the velocity fluctuations. The analogy between Bagnold's analysis and the kinetic theory of gases has led other researchers to develop kinetic theories for granular materials. Furthermore, the velocity fluctuations are referred to as *granular temperature* because of their similarity with the thermal motions of the molecules of a gas. The major difference between molecular interactions and those of the bulk solid's particles is that in the latter energy is dissipated. The computer approach commonly used to investigate dry flows of granular materials is the granular dynamics type of simulations. This numerical procedure is discrete in the sense that the movements of individual particles are studied.

3.2.2 Computer simulation of granular flows

The behaviour of granular flows developed in nature or in experiments is not well understood. This is primarily because of the difficulty of making measurements, in the laboratory or in industrial settings, of the interesting parameters, such as densities or velocities, without disturbing the flow. In computer simulations, this kind of problem is not encountered since the state of the system is known at all times. Recordings of the particles' positions, velocities and contact forces are used to obtain stress distributions or to determine the granular temperature of the system. An analysis of the instantaneous values of the different parameters can be done and good averages can also be computed.

In the domain of experiments, various types of problems have been investigated: uniform shear flows generated in an annular cell, chute flows down an inclined bed, the development of roll waves at the surface of a granular material flowing down a rough plane, and avalanches in rotating drums. Simulations of some of these experiments have been performed and their results have been compared with the experimental ones and also with the kinetic theories' predictions. Many of the simulations done involve two-dimensional flows where the particles are modeled as circular disks. In order to compare the 2-D simulations with the theoretical and experimental results, a relationship is established between the 2-D and the 3-D solids fractions based on an equivalent inter-particle spacing. Three-dimensional flows have also been simulated where the grains were considered to be spherical.

In computer simulations the motion of the individual particles is governed by Newton's laws. The particles collide with one another giving rise to normal and tangential contact forces. Between the collisions the particles follow a trajectory which is a function of time. An external force field such as gravity can be applied to the system. In granular dynamics simulations, the particles are treated as being hard or soft. The hard particle model implies instantaneous and binary collisions while the soft approach permits multiple contacts of a finite duration. The latter is more appropriate for high concentration flows in or close to the quasi-static regime. Different computational schemes are used depending on how the particles are modeled. The computational box in which the particles are enclosed can have two types of boundaries, either solid or periodic. The former are used when walls or beds are involved and the latter are applied when it is desired to increase significantly the computational region. Solid walls may consist of particles or they may be flat surfaces. The Lees-Edward boundary conditions are appropriate for the analysis of shear flows of infinite flow fields [Lees and Edward, 1972].

3.3 The actual computational formulation of the ice problem

3.3.1 Governing equations of motion; wind and water drag forces

The present model is concerned with deformations at the mesoscale; i.e. for length scales of the order of 100 km and time scales of the order of 2 days. The forces acting on sea ice at such scales are the wind and water drag as well as the Coriolis force. In addition to these three kinds of forcing, the ice floes are subjected to contact forces as was underlined in the previous chapter. The ice floes are considered to move in response to these forces and the equation of balance of momentum for a single floe can therefore be written as follows

$$m\frac{d\mathbf{u}}{dt} = -mf\mathbf{k}\times\mathbf{u} + A\boldsymbol{\tau}_a - A\boldsymbol{\tau}_w + \sum_{i=1}^{n}\mathbf{F}_i, \tag{43}$$

where $\mathbf{u}$ is the linear velocity, m is the mass of the ice floe, t is the time, $\mathbf{k}$ is a unit vector in the vertical direction, f is the Coriolis parameter, $\boldsymbol{\tau}_a$ and $\boldsymbol{\tau}_w$ are the air and water stresses, A is the floe area and $\sum_{i=1}^{n}\mathbf{F}_i$ is the vector sum of the n contact forces acting on the floe. The water shear stress is evaluated according to the linear drag law shown in equation (38) with a constant $C_w{}'$ of $0.0126\,\mathrm{kg\,m^{-2}\,s^{-1}}$ [Flato and Hibler, 1989]. Similarly, the wind shear stress is evaluated according to the linear drag law of equation (41) with $C_a{}'$ taken to be $0.652\,\mathrm{kg\,m^{-2}\,s^{-1}}$ [Flato and Hibler, 1989]. The wind and water drag forces are considered to act on the top and bottom surfaces of the ice floes.

The conservation of angular momentum, for a floe having a radius R, is based on the following equation

$$I\frac{d\omega}{dt} = \sum_{i=1}^{n} T_i - T_v \tag{44}$$

where I is the moment of inertia, which corresponds to $1/2\, m\, R^2$, ω is the angular velocity, $\sum_{i=1}^{n} T_i$ is the sum of the torques developed by the inter-particle contacts and T_v is the viscous resisting torque acting at the ice-water interface. The latter is expressed as follows [Savage, 1992]

$$T_v = \frac{\pi}{2} C_w \cos\beta\, \omega\, R^4. \tag{45}$$

Wind drag, water drag and the Coriolis force are assumed to act through the center of the floe and thus they induce no rotation. Only the torques arising from the collisions cause the floe to spin, and these rotational movements are resisted by the water shear stress at the floe's bottom surface.

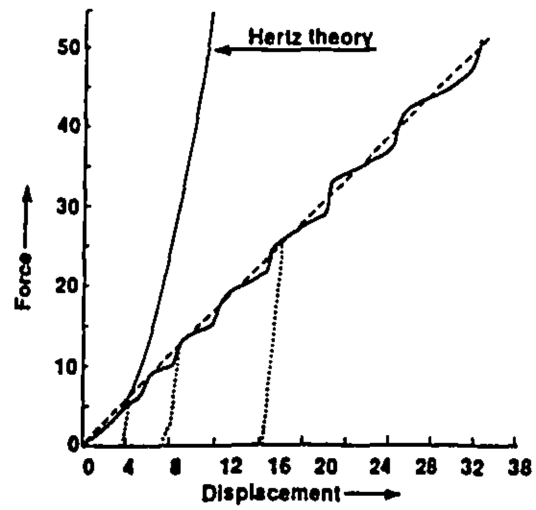

Figure 14: Loading and unloading force-displacement behaviour for elastic-plastic spheres during quasi-static normal displacement calculated using a finite element model [Walton, 1992].

3.3.2 Contact force models

Collisions with the soft particle model take place over many time steps during which energy is dissipated in the normal and tangential directions of the contacts. The normal contact forces between two particles are computed according to a force-displacement model. An elastic-perfectly-plastic constitutive model was used to determine the effective normal force displacement curve for a sphere impacting a wall [Walton, 1992]. The sphere was moved toward the wall, subsequently withdrawn, and then moved back to the wall again for several cycles in order to obtain the loading-unloading curve shown in Figure 14. From this graph we see that the loading and unloading forces are almost linearly dependent on the displacement with the unloading curve steeper than the loading one. The slope of the unloading curve increases linearly with the maximum contact force attained during loading. This behaviour suggests that collisions between

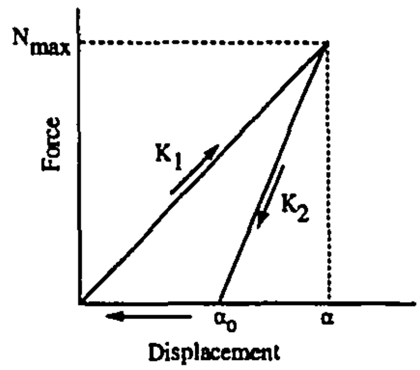

Figure 15: Force displacement diagram.

particles can be closely approximated by a linear spring acting between two rigid bodies. Walton and Braun [1986] presented a latching spring model that approximates the behaviour shown in Figure 14 and in which the normal forces are related to two different spring constants (Figure 15)

$$N = K_1\,\alpha \qquad \text{for loading,} \tag{46}$$

and

$$N = K_2\,(\alpha - \alpha_o) \qquad \text{for unloading,} \tag{47}$$

where α is the overlap of the two contacting particles and α_o is the value of α when N becomes zero. The energy dissipation corresponds to the area under the curve of Figure 15. The ratio of the moduli K_1 and K_2 is related to the restitution coefficient e, which is constant over the whole simulation, as follows

$$e = \sqrt{\frac{K_1}{K_2}} \tag{48}$$

Tangential forces are also considered to act at the interface between floes in a direction opposite to the relative tangential velocity. The magnitude of the tangential force T is calculated according to a Coulomb friction coefficient, $\mu = \tan \Phi$, such that

$$T = \mu N. \tag{49}$$

3.3.3 Boundary conditions and nondimensionalization

Situations involving different kinds of wind force fields have been simulated, these wind fields were either uniform, cyclonic or anti-cyclonic. For the cases where the wind field consists of a vortex the array of ice floes is enclosed by four solid boundaries. For the case of a uniform wind, a solid boundary is placed at the right hand side, a free boundary occurs on the left, and periodic boundaries are applied in the direction of the flow. Computations conducted under these conditions will be presented in a later chapter.

It is convenient to use a dimensionless form of the governing equations in the computations. Comparisons with field conditions or with other studies can be easily done afterwards. The largest floe diameter D is used as a reference length. Time and velocity reference values are respectively taken to be $\sqrt{M/K_1}$ and $D/\sqrt{M/K_1}$, where M is the mass of the largest floe [Savage, 1992]. In the preliminary computations, the material property values were taken to be: $K_1 = 2.5 \times 10^5$ N/m, $\rho = 0.91 \times 10^3$ kg/m^3, $\mu = 0.3$, and e varied from 0.2 to 0.8.

3.3.4 Program logic

A number of particles are located in a rectangular array bounded by two or four rough walls depending on the wind conditions. Initially, each particle is given a small random velocity. Wind and water drag cause the motion to begin, and, after a short period of time, collisions occur giving rise to contact forces.

A short time interval is used in order to have several time steps during each collision. The neighbors of each particle are regularly checked for contacts. The overlapping distance of two particles, α, is calculated and, depending on whether the particles are approaching or retreating from each other, K_1 or K_2 is used in the evaluation of the contact force. The tangential force is then computed after determining the direction of the relative tangential velocity. Forces from all contacts are then added for each particle and the equations of balance of momentum are integrated over the time step in order to give the particles new positions and velocities. The calculations are repeated for the following time steps .

3.4 References

Bagnold, R.A 1954. Experiments on a gravity free dispersions of large solid spheres in a Newtonian fluid under shear. *Proc. R. Soc. London, Ser. A*, **225**, 49-63.

Flato, G.M. and Hibler, W.D. 1989. The effect of ice pressure on marginal ice zone dynamics. *IEEE Trans. on Geoscience and Remote Sensing*, **27**, 514-521.

Leppäranta, M. and Hibler, W.D. 1987. Mesoscale sea ice deformation in the East Greenland marginal ice zone. *J. Geophys. Res.*, **92**, 7060-7070.

Jaeger, H.M. and Nagel, S.R. 1992. La physique de l'état granulaire. *La Recherche*, **23**, 1380-1387.

Lees, A.W. and Edwards, S.F. 1972. The computer study of transport processes under extreme conditions. *J. Phys.*, **C5**, 1921-1929.

Savage, S.B. 1992. Marginal ice zone dynamics modelled by computer simulations involving floe collisions. Report for the contract 91-1547/5471, prepared for the IME of the National Research Council Canada.

Walton, O.R. and Braun, R.L. 1986. Viscosity and temperature calculations for assemblies of inelastic frictional disks. *J. Rheology*, **30**, 949-980.

Walton, O.R. 1992. Numerical simulation of inelastic frictional particle-particle interactions, *Particulate Two-Phase Flow*, edited by Roco, M.C., Butterworth-Heinemann, Boston, 884-907.

4 Non-Linear Effects of Water and Air Drag

4.1 Introduction

In §2.3.1 we showed how the drag exerted by the water and by the wind on the horizontal surfaces of the ice floes is evaluated. The air shear stress is determined using the following linear relationship

$$\tau_a = C_a{}' \, B_\alpha \, \mathbf{V}_a \tag{50}$$

where $C_a{}'$ is a constant, $\mathbf{V}_a$ is the wind velocity and B_α is a matrix involving the boundary layer turning angle α, i.e. the angle between the air stress vector and the direction of the geostrophic wind

$$B_\alpha = \begin{pmatrix} \cos\alpha & -\sin\alpha \\ \sin\alpha & \cos\alpha \end{pmatrix}.$$

In a similar fashion the water shear stress resisting the motion of the floe is expressed as

$$\tau_w = C_w{}' \, B_\beta \, \mathbf{u} \tag{51}$$

where $C_w{}'$ is the linear water drag coefficient, $\mathbf{u}$ is the ice floe velocity, and β is the angle between the water stress vector and the ice velocity vector relative to the geostrophic current. It is assumed that the water current velocity outside the viscous boundary layer is negligible compared to the ice floe velocity $\mathbf{u}$.

A more realistic water shear stress would be proportional to the square of the relative velocity between the ice floe and the water current. The use of a quadratic drag law no longer allows the effects of the floe spin and of the translational motion to be superposed. The development of expressions for the water drag force and for the viscous resisting torque, using quadratic relationships to relate the stresses to the relative velocities, is presented in this section. In a similar fashion an expression for the wind drag force is derived. The new formulations of the stresses require the appropriate dimensionless wind and water drag coefficients. A literature review of these drag coefficients is presented along with the analyses.

4.2 Water drag force

The two components of the water shear stress acting on the bottom surface of an individual ice floe can be written as follows

$$\tau_{wx} = \rho_w C_w \cos\beta \, |\mathbf{V}_w - \mathbf{V}| \, (V_{wx} - V_x) - \rho_w C_w \sin\beta \, |\mathbf{V}_w - \mathbf{V}| \, (V_{wy} - V_y), \quad (52)$$

$$\tau_{wy} = \rho_w C_w \sin\beta \, |\mathbf{V}_w - \mathbf{V}| \, (V_{wx} - V_x) + \rho_w C_w \cos\beta \, |\mathbf{V}_w - \mathbf{V}| \, (V_{wy} - V_y). \quad (53)$$

In the previous equations ρ_w is the water density, $\mathbf{V}_w$ is the water current velocity, and $\mathbf{V}$ is the linear velocity at a particular point on the floe. The latter consists of the velocity of the center of gravity, $\mathbf{V}_{cg}$, to which is added the contribution due to the floe rotation. These velocity vectors are sketched in Figure 16a. A small elemental area dA with a force vector dF acting on it is represented in Figure 16b. The two contributions of the velocity vector of this element are sketched in Figure 16c as well as the water velocity vector. Values of C_w, the quadratic drag coefficient, for different types of ice and for water currents measured at different depths are given in Table 1.

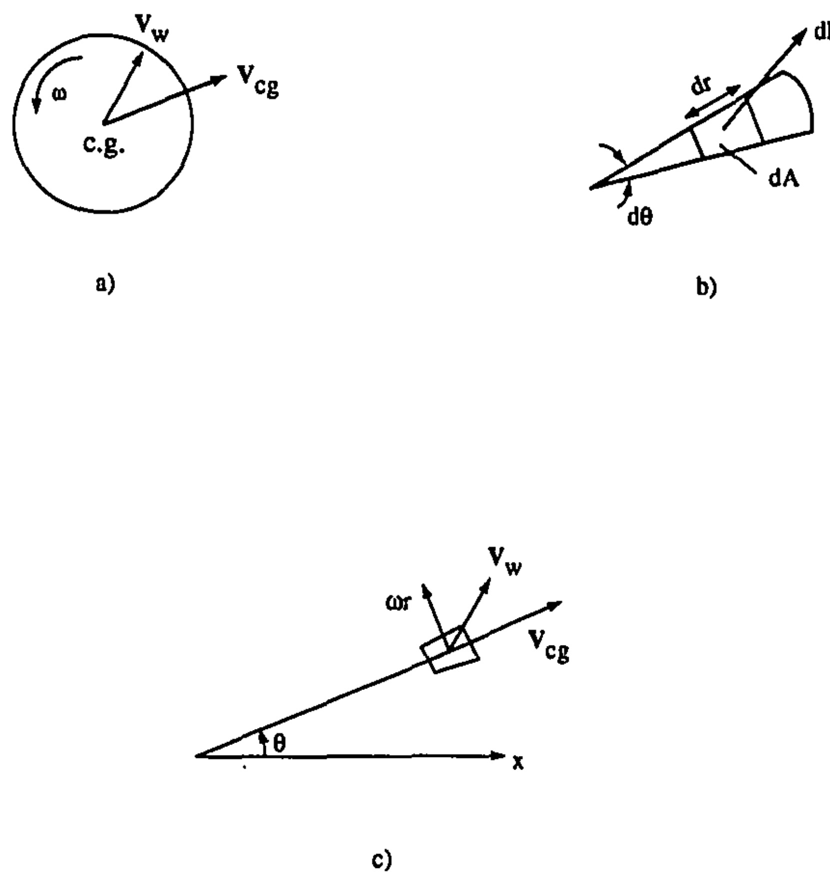

Figure 16: Diagram defining coordinate systems, velocity vectors and elemental areas.

The geostrophic depth is the depth at which the frictional effects induced by the wind blowing on the water surface, or on the ice floes, vanish and where the current is established by the Coriolis and pressure gradient forces. The turning angle β associated with the geostrophic current was evaluated by McPhee [1980] and by McPhee and Smith [1976]; it appears that β is consistent from year to year and that it has an average value of 24°. McPhee [1978, 1979] has performed an investigation on turning angles related to water currents measured within the viscous layer but the results he obtained were not reliable due to large errors in current meter measurements and directions. This suggests that the water stresses and their directions should be evaluated using geostrophic or surface currents since the values of the turning angles for other water depths are not known. When surface currents are involved, the turning angle is zero since the stresses act in the direction of the ice velocity relative to the surface current.

Investigator	Ice Type	Reference Depth (m)	$C_w \times 10^3$
McPhee and Smith [1976]	smooth	geostrophic	3.40
McPhee [1980]	rough	geostrophic	5.50
McPhee [1979]	rough	2.0	20.00
Madsen and Bruno [1986]	smooth	2.0	5.46
Madsen and Bruno [1986]	rough	2.0	15.00
Madsen and Bruno [1986]	slighty rough	5.1	4.07
Madsen and Bruno [1986]	slighty rough	1.1	8.40

Table 1: Representative values of the water drag coefficients.

For the time being, we will take the turning angle to be zero such that the two components of the elemental force acting on a small element dA are the following

$$dF_x = \rho_w \, C_w \, |\mathbf{V}_w - \mathbf{V}| \, (V_{wx} - V_x) \, r \, dr \, d\theta, \tag{54}$$

$$dF_y = \rho_w \, C_w \, |\mathbf{V}_w - \mathbf{V}| \, (V_{wy} - V_y) \, r \, dr \, d\theta. \tag{55}$$

This assumption is only temporary and is made in order to simplify a number of terms involved in the derivation of the drag force. The computer program used to conduct the simulations integrates the equations of motion for the x and y directions and consequently we must express the drag forces in terms of their x and y components. The force components F_x and F_y are determined by integrating dF_x and dF_y over the floe area. In order to reduce the number of terms involved in the integrations another reference axis is chosen. The new x axis, which we will call x', is along the vector $\mathbf{V}_w - \mathbf{V}_{cg}$. Since the angles that $\mathbf{V}_w$ and $\mathbf{V}_{cg}$ make with the x axis are known ($\mathbf{V}_w$ is constant throughout the computer simulation and $\mathbf{V}_{cg}$ is computed at every time step), the angle by which the reference axes are shifted can be expressed in terms of these two vectors and of their angles. Defining ζ as being the angle between $\mathbf{V}_{cg}$ and the x axis, ϵ as the angle between $\mathbf{V}_w$ and the x axis then γ, the angle formed by $\mathbf{V}_w - \mathbf{V}_{cg}$ and the x axis is expressed as follows

$$\gamma = \arctan \frac{|\mathbf{V}_w| \sin \epsilon - |\mathbf{V}_{cg}| \sin \zeta}{|\mathbf{V}_w| \cos \epsilon - |\mathbf{V}_{cg}| \cos \zeta}. \tag{56}$$

The new set of axes as well as the vector $\mathbf{V}_w - \mathbf{V}_{cg}$ are shown in Figure 17. The

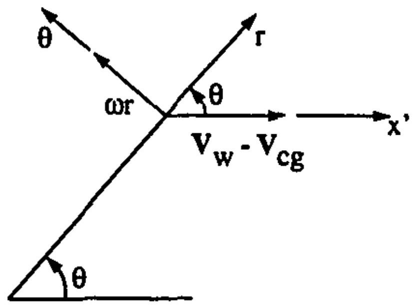

Figure 17: Diagram defining the x' coordinate system.

magnitude of $\mathbf{V}_w - \mathbf{V}_{cg}$ corresponds to

$$|\mathbf{V}_w - \mathbf{V}_{cg}| \;=\; \sqrt{\mathbf{V}_{cg}^2 - 2|\mathbf{V}_{cg}||\mathbf{V}_w|\cos(\epsilon - \zeta) + \mathbf{V}_w^2}. \tag{57}$$

The relative velocity vector, $\mathbf{V}_w - \mathbf{V}$, needed to find the x' and y' components of the force, is expressed in terms of its θ and r components in the following equation

$$\mathbf{V}_w - \mathbf{V} = (-\omega r - |\mathbf{V}_c|\sin\theta)\ \mathbf{e}_\theta + |\mathbf{V}_c|\cos\theta\ \mathbf{e}_r, \tag{58}$$

where $\mathbf{V}_c$ corresponds to $\mathbf{V}_w - \mathbf{V}_{cg}$. An equivalent way to write $dF_{x'}$ and $dF_{y'}$ is the following

$$dF_{x'} \;=\; \rho_w\ C_w\ (\mathbf{V}_w - \mathbf{V})^2\ \cos\eta\ r\ dr\ d\theta, \tag{59}$$

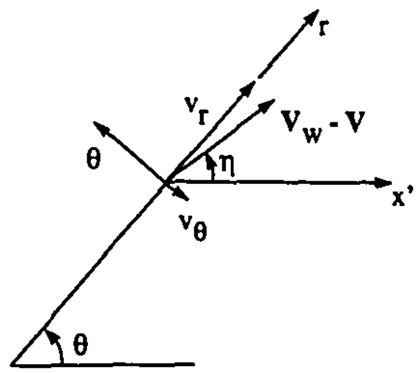

Figure 18: Diagram defining velocity vectors on the x' coordinate system.

$$dF_{y'} = \rho_w \, C_w \, (\mathbf{V}_w - \mathbf{V})^2 \, \sin\eta \, r \, dr \, d\theta \tag{60}$$

where η is the angle that $\mathbf{V}_w - \mathbf{V}$ makes with the x' axis. By looking at Figure 18, it can be seen that

$$\cos(\eta - \theta) = \frac{v_r}{|\mathbf{V}_w - \mathbf{V}|}, \tag{61}$$

and

$$\sin(\eta - \theta) = \frac{v_\theta}{|\mathbf{V}_w - \mathbf{V}|}. \tag{62}$$

Combining these two equations, we obtain

$$\cos\eta = \frac{v_r \cos\theta + v_\theta \sin\theta}{|\mathbf{V}_w - \mathbf{V}|}, \tag{63}$$

$$\sin\eta = \frac{v_r \sin\theta + v_\theta \cos\theta}{|\mathbf{V}_w - \mathbf{V}|}. \tag{64}$$

Substituting for v_θ and for v_r, the previous equations become

$$\cos\eta = \frac{2\,|\mathbf{V}_c|\cos^2\theta - |\mathbf{V}_c| - \omega r \sin\theta}{|\mathbf{V}_w - \mathbf{V}|}, \tag{65}$$

$$\sin\eta = \frac{-\omega r \cos\theta}{|\mathbf{V}_w - \mathbf{V}|}. \tag{66}$$

We can now write the expressions for $dF_{x'}$ and $dF_{y'}$

$$dF_{x'} = \rho_w\, C_w \sqrt{\omega^2 r^2 + 2\omega r |\mathbf{V}_c| \sin\theta + |\mathbf{V}_c|^2}\ \left(-|\mathbf{V}_c| - \omega r \sin\theta + 2|\mathbf{V}_c|\cos^2\theta\right) r\, dr\, d\theta \tag{67}$$

$$dF_{y'} = \rho_w\, C_w \sqrt{\omega^2 r^2 + 2\omega r |\mathbf{V}_c| \sin\theta + |\mathbf{V}_c|^2}\ \left(-\omega r \cos\theta\right) r\, dr\, d\theta. \tag{68}$$

We can divide $dF_{x'}$ into three components

$$dF_1 = \rho_w\, C_w \sqrt{\omega^2 r^2 + 2\omega r |\mathbf{V}_c| \sin\theta + |\mathbf{V}_c|^2}\ \left(-|\mathbf{V}_c|\right) r\, dr\, d\theta, \tag{69}$$

$$dF_2 = \rho_w\, C_w \sqrt{\omega^2 r^2 + 2\omega r |\mathbf{V}_c| \sin\theta + |\mathbf{V}_c|^2}\ \left(-\omega r \sin\theta\right) r\, dr\, d\theta, \tag{70}$$

$$dF_3 = \rho_w\, C_w \sqrt{\omega^2 r^2 + 2\omega r |\mathbf{V}_c| \sin\theta + |\mathbf{V}_c|^2}\ \left(2\,|\mathbf{V}_c|\cos^2\theta\right) r\, dr\, d\theta. \tag{71}$$

There is no closed form solution to the integrals of equations (68) to (71), so we must integrate them numerically. In order to do this numerical integration, the nondimensionalization of the variable r was required. This variable was nondimensionalized by R, the radius of the floe for which the force is to be calculated, yielding a new variable z which corresponds to r/R and ranges from 0 to 1. The first component, dF_1, of the elemental force can be written as follows

$$dF_1 = -\rho_w \, C_w \, |\mathbf{V}_c| \frac{r}{R} R^3 \omega \sqrt{\frac{\omega^2 r^2}{\omega^2 R^2} + \frac{2\omega r |\mathbf{V}_c| \sin\theta}{\omega^2 R^2} + \frac{|\mathbf{V}_c|^2}{\omega^2 R^2}} \, d\frac{r}{R} \, d\theta, \tag{72}$$

and finally in terms of z and of a new parameter G corresponding to $|\mathbf{V}_c|/\omega R$, dF_1 takes on the following form

$$dF_1 = -\rho_w \, C_w \, |\mathbf{V}_c| \, R^3 \, \omega \, z \sqrt{z^2 + 2\, G\, z \, \sin\theta + G^2} \, dz \, d\theta. \tag{73}$$

In a similar fashion dF_2, dF_3 and $dF_{y'}$ are expressed as follows

$$dF_2 = -\rho_w \, C_w \, \omega^2 \, R^4 \, z^2 \, \sin\theta \sqrt{z^2 + 2\, G\, z \, \sin\theta + G^2} \, dz \, d\theta, \tag{74}$$

$$dF_3 = 2\, \rho_w \, C_w \, |\mathbf{V}_c| \, R^3 \, \omega \, z \cos^2\theta \sqrt{z^2 + 2\, G\, z \, \sin\theta + G^2} \, dz \, d\theta, \tag{75}$$

$$dF_{y'} = -\rho_w \, C_w \, \omega^2 \, R^4 \, z^2 \, \cos\theta \sqrt{z^2 + 2\, G\, z \, \sin\theta + G^2} \, dz \, d\theta. \tag{76}$$

The parts of dF_1, dF_2, dF_3 and $dF_{y'}$ that contain the variables z and θ will be called $d\tilde{F}_1, d\tilde{F}_2$, $d\tilde{F}_3$ and $d\tilde{F}_{y'}$ respectively.

$$d\tilde{F}_1 = z \sqrt{z^2 + 2\, G\, z \, \sin\theta + G^2} \, dz \, d\theta, \tag{77}$$

$$d\tilde{F}_2 = z^2 \sin\theta\sqrt{z^2 + 2\,G\,z\,\sin\theta + G^2}\,dz\,d\theta, \tag{78}$$

$$d\tilde{F}_3 = z\cos^2\theta\sqrt{z^2 + 2\,G\,z\,\sin\theta + G^2}\,dz\,d\theta, \tag{79}$$

$$d\tilde{F}_{y'} = z^2\cos\theta\sqrt{z^2 + 2\,G\,z\,\sin\theta + G^2}\,dz\,d\theta. \tag{80}$$

The above expressions were integrated numerically for θ ranging from 0 to 2π and z varying from 0 to 1. The integrals were computed for several values of G. The integral of $dF_{y'}$ was found to be zero for any value of G. This result was to be expected since the elemental forces acting in the y' direction are uniquely related to the angular velocity of the disk. The results obtained from the integration of each of the three components of $dF_{x'}$ were plotted against the parameter G. A public domain software SciPlot was used to determine functions that fit each of these curves. These functions are written below

$$\int_0^{2\pi}\int_0^1 d\tilde{F}_1 \approx -0.3147 + 3.1754\sqrt{0.5349 + G^2}, \tag{81}$$

$$\int_0^{2\pi}\int_0^1 d\tilde{F}_2 \approx 0.78\tanh(1.5016\,G), \tag{82}$$

$$\int_0^{2\pi}\int_0^1 d\tilde{F}_3 \approx -0.0193 + 1.5716\,\sqrt{0.4466 + G^2}. \tag{83}$$

The numerical results obtained from the numerical integration of $d\tilde{F}_1, d\tilde{F}_2$, $d\tilde{F}_3$ and $d\tilde{F}_{y'}$ are plotted in Figures 19 to 21 with their respective curve fits. Now that the three force components are evaluated, $F_{x'}$ can be written in the following manner

$$\begin{aligned} F_{x'} \approx\; & \rho_w\, C_w[-|\mathbf{V}_c|\,R^3\,\omega\,(-0.3147 + 3.1754\sqrt{0.5349 + G^2}) - \omega^2\,R^4\,0.78\tanh(1.5016\,G) \\ & +\; 2\,|\mathbf{V}_c|\,R^3\,\omega\,(-0.0193 + 1.5716\,\sqrt{0.4466 + G^2})\,]. \end{aligned} \tag{84}$$

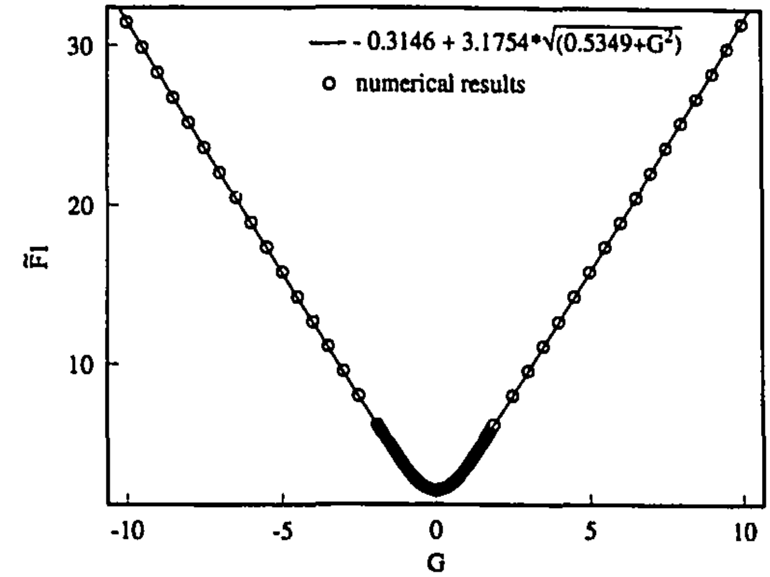

Figure 19: Numerical values of the elemental force $\tilde{F}_1$, as a function of the parameter G.

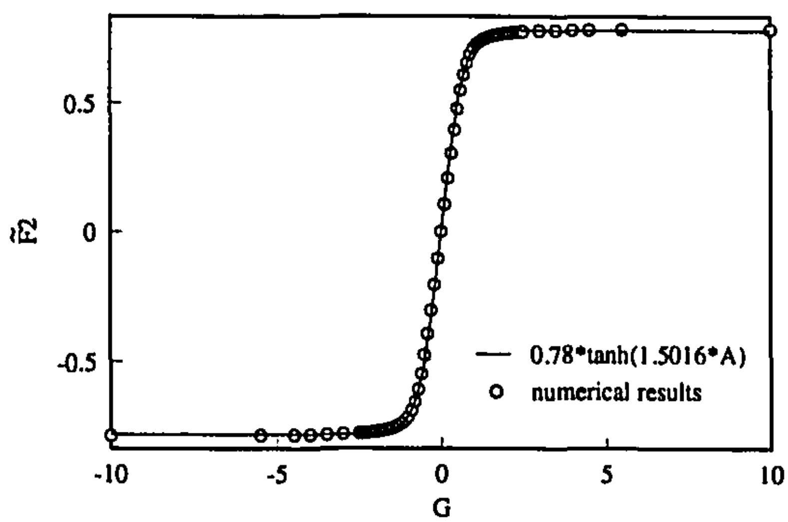

Figure 20: Numerical values of the elemental force $\tilde{F}_2$, as a function of the parameter G.

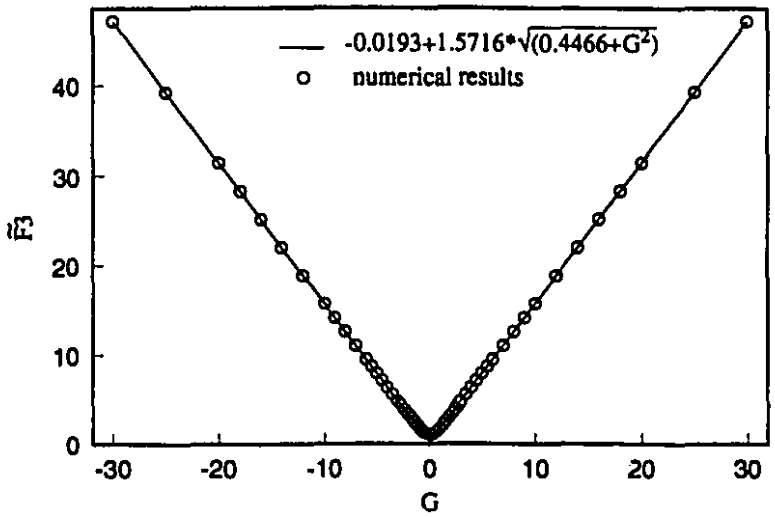

Figure 21: Numerical values of the elemental force $\tilde{F_3}$, as a function of the parameter G.

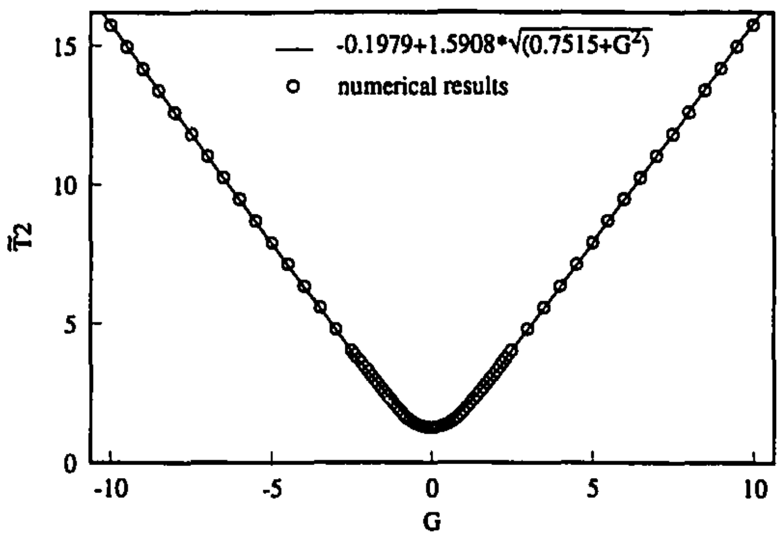

Figure 22: Numerical values of the elemental force $\tilde{T_2}$, as a function of the parameter G.

Writing the previous equation in terms of $\omega, |\mathbf{V}_c|$, and R we obtain

$$\begin{aligned}
F_{x'} &\approx \rho_w\, C_w\, [\,0.3147\, |\mathbf{V}_c|\, R^3 \omega - 3.1754 \sqrt{0.5349\, |\mathbf{V}_c|^2 R^6 \omega^2 \;+\; |\mathbf{V}_c|^4 R^4} \\
&- \omega^2 R^4\, 0.78 \tanh(1.5016 \frac{|\mathbf{V}_c|}{\omega r}) - 0.0386\, |\mathbf{V}_c|\; R^3\, \omega \\
&+ 3.1432\, \sqrt{0.4466\, |\mathbf{V}_c|^2\, R^6\, \omega^2 + \; |\mathbf{V}_c|^4\, R^6}\,]. \qquad (85)
\end{aligned}$$

For an ice floe having a zero rotational velocity, the above equation reduces to $-3.1754\, R^2\, \rho_w\, C_w\, |\mathbf{V}_c|^2$ which is very close to the exact expression $-\pi\, R^2\, \rho_w\, C_w\, |\mathbf{V}_c|^2$. The last step in our derivation is to shift back the axes in order to obtain the proper components of the water drag force. This can be done by multiplying $F_{x'}$ by the cosine of γ to obtain F_x, and by $\sin\gamma$ to obtain F_y. Furthermore, the effects of the viscous boundary layer must be included if geostrophic currents are used in the simulations. This is done by reintegrating the turning angle β which had been neglected temporarily. Finally, we obtain for F_x and F_y the following expressions

$$F_x \;=\; \cos\beta\;\, \cos\gamma\; F_{x'} \;-\; \sin\beta\;\, \sin\gamma\; F_{x'}, \qquad (86)$$

$$F_y \;=\; \sin\beta\;\, \cos\gamma\; F_{x'} \;+\; \cos\beta\;\, \sin\gamma\; F_{x'}. \qquad (87)$$

4.3 Viscous resisting torque

The torques arising from collisional contacts with neighboring ice floes are resisted by the water shear stress on the bottom of the ice floe. The elemental torque resisting the spin of the floe is equal to r, the arm, multiplied by dF_θ, the component of the elemental force in the θ direction. Since $dF_\theta = \tau_\theta\ r\ dr\ d\theta$, the elemental torque can be written as

$$dT \;=\; \tau_\theta\ r^2\ dr d\theta \tag{88}$$

where

$$\tau_\theta = \rho_w\ C_w\,|\mathbf{V}_w - \mathbf{V}|(v_\theta \cos\beta - v_r \sin\beta). \tag{89}$$

Substituing for v_r and v_θ the stress in the θ direction can be expressed as

$$\tau_\theta = \rho_w\ C_w\ \sqrt{\omega^2 r^2 + 2\omega r|\mathbf{V}_c|\sin\theta + |\mathbf{V}_c|^2}\ [(-\omega r - |\mathbf{V}_c|\sin\theta)\cos\beta - |\mathbf{V}_c|\cos\theta\sin\beta]. \tag{90}$$

The elemental torque can be divided into three components

$$dT_1 = -\rho_w\ C_w\ \cos\beta\ \omega\, r^3\ \sqrt{\omega^2 r^2 + 2\omega r|\mathbf{V}_c|\sin\theta + |\mathbf{V}_c|^2}\ dr\ d\theta, \tag{91}$$

$$dT_2 = -\rho_w\ C_w\ \cos\beta\ |\mathbf{V}_c|\ r^2\ \sin\theta\ \sqrt{\omega^2 r^2 + 2\omega r|\mathbf{V}_c|\sin\theta + |\mathbf{V}_c|^2}\ dr\ d\theta, \tag{92}$$

$$dT_3 = -\rho_w\ C_w\ \sin\beta\ |\mathbf{V}_c|\ r^2\ \cos\theta\ \sqrt{\omega^2 r^2 + 2\omega r|\mathbf{V}_c|\sin\theta + |\mathbf{V}_c|^2}\ dr\ d\theta. \tag{93}$$

After nondimensionalization of r we find

$$dT_1 = -\rho_w \, C_w \, \cos\beta \, \omega^2 \, R^5 \, z^3 \, \sqrt{z^2 + 2\,G\,z\,\sin\theta + G^2} \, dz \, d\theta, \tag{94}$$

$$dT_2 = -\rho_w \, C_w \, \cos\beta \, |\mathbf{V}_c| \, \omega \, R^4 \, z^2 \, \sin\theta \, \sqrt{z^2 + 2\,G\,z\,\sin\theta + G^2} \, dz \, d\theta, \tag{95}$$

$$dT_3 = -\rho_w \, C_w \, \sin\beta \, |\mathbf{V}_c| \, \omega \, R^4 \, z^2 \, \cos\theta \, \sqrt{z^2 + 2\,G\,z\,\sin\theta + G^2} \, dz \, d\theta. \tag{96}$$

The part of dT_3 containing the z and θ terms, $d\tilde{T}_3$, is identical to $d\tilde{F}_{y'}$ and is therefore equal to zero when integrated. Moreover, we observe that $d\tilde{T}_2$ corresponds to $d\tilde{F}_2$. After curve fitting the values obtained by the numerical integration of $d\tilde{T}_1$, the following function was found to fit the results

$$\int_0^{2\pi}\int_0^1 z^3\sqrt{z^2 + 2\,G\,z\,\sin\theta + G^2}\,dz\,d\theta \approx -0.1979 + 1.5908\,\sqrt{0.7515 + G^2}. \tag{97}$$

The numerical results and the above function are plotted in Figure 22. The expression for the torque developed in this section is not affected by the rotation of the axes by the angle γ and consequently it does not need to be modified. The torque is to be evaluated using the following expression

$$T \approx \rho_w \, C_w \, \cos\beta \, [\, -\omega^2 R^5(-0.1979 + 1.5908\,\sqrt{0.7515 + G^2}) - |\mathbf{V}_c|\,\omega R^4(0.78\,\tanh(1.5016\,G))\,], \tag{98}$$

and in terms of $|\mathbf{V}_c|$, ω, and R, the above equation becomes

$$
\begin{aligned}
T \;\approx\; & \rho_w\, C_w\, \cos\beta\, [0.1979\, \omega^2\, R^5 \;-\; 1.5908\, \sqrt{0.7515\, \omega^4\, R^{10} \;+\; |\mathbf{V}_c|^2\, \omega^2\, R^6} \\
& -\; 0.78\, |\mathbf{V}_c|\, \omega\, R^4 \tanh(1.5016\, \frac{|\mathbf{V}_c|^2}{\omega^2 R^2})]. \qquad (99)
\end{aligned}
$$

4.4 Air drag force

The ice speed corresponds to only 3 to 5 percent of the wind's speed and thus it is not necessary to use the relative velocity vector between the air and the ice floe in the calculations of the stresses. The x and y components of the air drag force are given by the following relationships

$$F_{ax} \;=\; \rho_a\, C_a\;\; 2\pi R^2\, |\mathbf{V}_a|\, [\cos\alpha\; u_a \;-\; \sin\alpha\; v_a], \qquad (100)$$

$$F_{ay} \;=\; \rho_a\, C_a\; 2\pi R^2\, |\mathbf{V}_a|\, [\sin\alpha\; u_a \;+\; \cos\alpha\; v_a], \qquad (101)$$

where ρ_a is the air density, C_a is the dimensionless air drag coefficient, and u_a and v_a are the x and y components of $\mathbf{V}_a$, the wind velocity. The drag coefficients are usually evaluated from winds measured at the standard anemometer height which is 10 m. A literature review of the drag coefficients evaluated from several studies is presented in Overland [1985]. The 10-m drag coefficients reported by 28 studies vary from 1.2×10^{-3} to 3.7×10^{-3}. The lowest values correspond to a smooth ice surface and the largest to rough ice. Overland [1985] has observed that the nature of the ice surface is not the sole characteristic influencing the amount of drag exerted by the wind. Indeed, the concentration of ice on the water surface, the air temperature, the stability of the atmosphere and the size of the ice floes are important factors in the determination of drag coefficients. Overland [1985] has grouped in a table (Table 2) the 10-m drag coefficients for smooth ice, for the Arctic pack, for the marginal seas, and for the inner and outer marginal ice zones (MIZ).

Ice Regime	Characteristics	$T_a \sim 0°$	$T_a < -5°$, $Z_i < 300$ m	$T_a < -5°$, $Z_i > 400$ m
Smooth ice	large, flat floes	1.5[a]	1.5[b]	
Arctic pack	large range of floe sizes, large pressure ridges, C_i >0.9	1.7[c]	2.6[d,e]	
Marginal seas	broken, first-year ice, C_i = 0.9, occasional big floes	2.2[f]	2.7[g]	3.0[h]
Inner MIZ	small floes, rafted, C_i = 0.8–0.9	2.6[i]	3.0[j]	3.7[k]
Outer MIZ	C_i = 0.4	2.2[l]		
	C_i = 0.3, rubble field	2.8[m]		

Table 2: Composite table of air drag coefficients referred to 10-m winds ($10^3 C_a$) as a function of ice and meteorological regime [Overland, 1985].

For a specific environment, the drag coefficients are expressed as a function of the meteorological regime. From this table we can observe that the drag coefficients increase as the floe size decreases and that for the same type of ice cover the drag coefficient increases for temperatures below $-5°$ C and for an atmospheric boundary layer not constrained by a low inversion height, Z_i. Overland [1985] defines large floes as those having lengths of the order of 1 km or more. The marginal ice zone is a region close to the open water in which the ice floes have more rounded features than in other regions. The data reported by Overland [1985] are for the MIZ of Greenland and for the Bering Sea. Marginal seas include the Gulf of Saint-Lawrence away from the MIZ, the coastal Beaufort sea, Bothnia Sea and Bay, the northern Sea of Okhotsk and Bering Sea and the Robeson Channel.

When the surface drag coefficient is known, the geostrophic drag coefficient can be derived using the following relationship

$$C_a = C_{10}\,({V_{10}}^2/{V_a}^2). \tag{102}$$

In Figure 23 are plotted the air stresses evaluated using surface and geostrophic winds for the Caribou station of AIDJEX [Coon, 1980]. The stresses were computed for a 20-day period. The 10-m drag coefficient was taken to be 2.7×10^{-3}. For the stresses computed with the geostrophic wind, a turning angle of 25° was used and C_a was calculated using equation (102) with the 20-day mean of $({V_{10}}^2/{V_a}^2)$. As illustrated in Figure 23, the stresses calculated with both types of wind are in very good agreement.

4.5 Summary and concluding remarks

Simple expressions were developed to evaluate the drag exerted by the water and by the air on individual ice floes in the most accurate manner. These drag forces have to be evaluated at every time step in the course of the simulations. The water drag has two contributions; one resisting the translational motion of the floe and the other its spin. Equation (86) must be used to evaluate the x component of the drag force while the y component is given by equation (87). The final equation for the water resisting torque is given by equation (98). The x and y components of the air drag are given by equation (100) and (101), respectively.

The linear relationships that are currently used to conduct the computer simulations

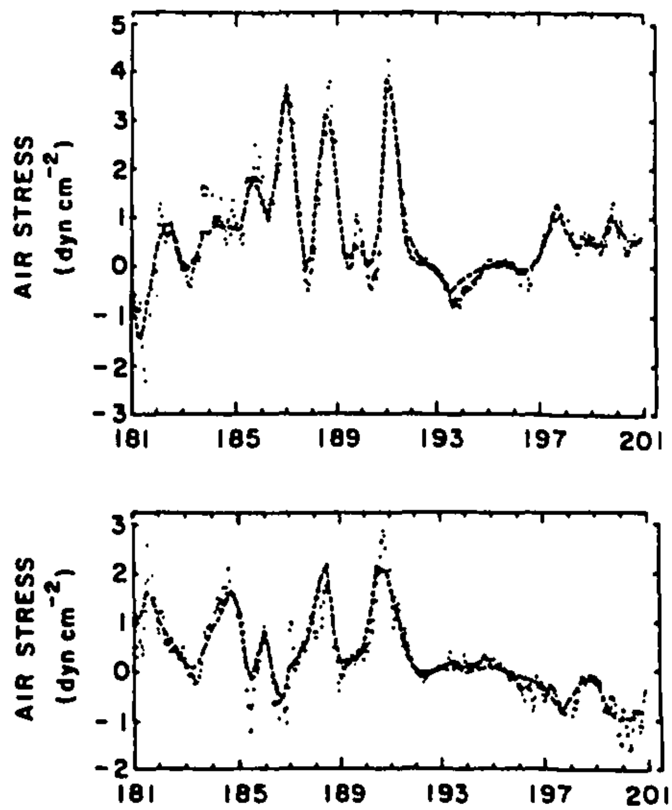

Figure 23: Air stress for Caribou, days 181-201 (30 June-20 July 1975). Upper plot, east-west component; lower plot, north-south component. Data points are from surface winds and the line is from geostrophic winds [Coon, 1980].

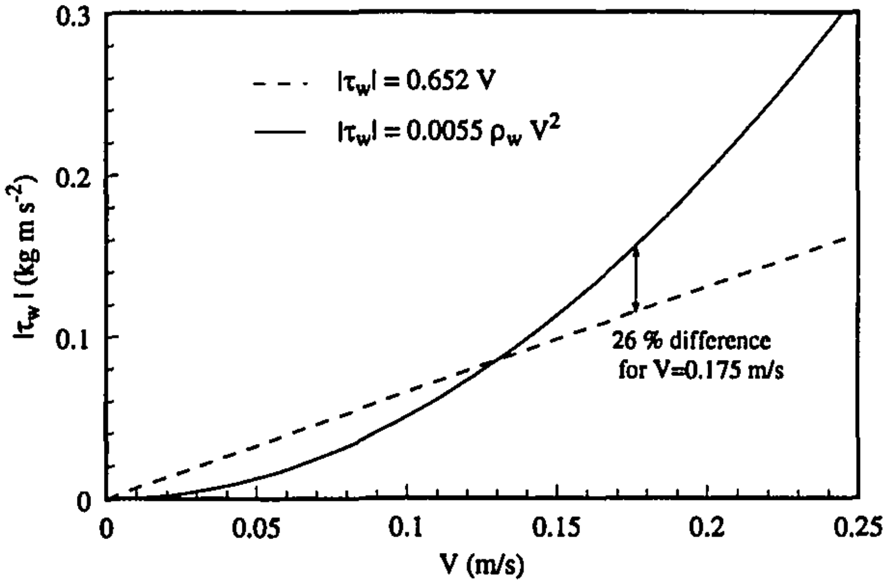

Figure 24: Water stress versus relative ice speed.

tions are appropriate for winds close to 10 m/s and for ice velocities relative to the water current of approximately 0.1 m/s. Some computer simulations, involving a linear drag law, were performed for a rectangular array of ice floes with a solid boundary on one side. There is a geostrophic wind blowing parallel to this boundary at a velocity of 10 m/s and there is no geostrophic water current. High concentrations of ice develop close to the solid boundary due to the fact that the Coriolis force, which acts perpendicularly to the velocity, pushes the floes toward this direction. A spatial and time averaged floe velocity of 0.175 m/s was calculated. This velocity is much larger than the expected value of 0.1 m/s. In Figure 24 are plotted the water stresses evaluated from the two relationships, linear and quadratic. From this figure we can see that the water stresses calculated in the simulations, using the linear drag law, were underestimated by 26 percent. This difference is not negligible and it appears that it

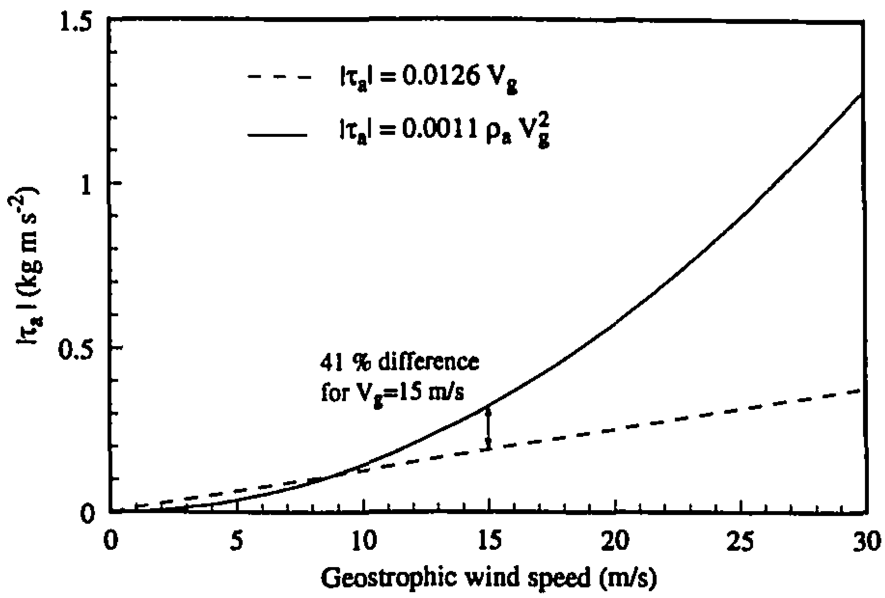

Figure 25: Wind stress versus geostrophic wind speed.

is not an easy task to determine in advance what the ice velocity will be.

Fissel and Tang [1991] present in their paper *Response of sea ice drift to wind forcing on the Northeastern Newfoundland Shelf*, geostrophic winds that were derived from meteorological data for 1988. Their data show that the geostrophic wind speed was uniformly distributed from a few m/s to 30 m/s. In Figure 25 are plotted the air stresses, evaluated according to both relationships, for geostrophic wind speed varying from 0 to 30 m/s. From this graph, we observe that a variation of the wind speed from 10 to 15 m/s yields an error of 41 percent in the stresses calculated with the linear relationship. The model that we are currently developing will be used to predict the movements of ice floes over lengths of the order of 100 km and for periods of a few days. During such short periods of time, high variations in the wind's speed strongly affects the ice motion and the model must be able to adequately reflect these effects.

Moreover, the winds over regions of this length scale are not likely to be uniform; that is the case for a vortex wind field where the wind is very strong at the center of the vortex and decreases with radial distance. There can be a factor of three or more between the magnitude of the wind at the center and that at the margin. It appears from these examples that the linear drag laws, which were developed for large time and length scale models, are not suitable for the problems in the present study. Therefore, the relatively simple quadratic relationships derived in this chapter should be incorporated in the discrete element model as soon as possible in order to obtain the most reliable results.

4.6 References

Banke, E.G. and Smith, S.D. 1971. Wind stress over ice and over water in the Beaufort Sea. *J. Geophys. Res.*, **76**, 7368-7374.

Banke, E.G. and Smith, S.D. and Anderson, J. 1976. Recent measurements of wind stress on arctic sea ice. *J. Fish. Res. Board. Can.*, **33**, 2307-2317.

Coon M.D. 1980. A Review of AIDJEX Modeling. *Sea Ice Processes and Models*, edited by R.S. Pritchard, University of Washington Press, Seattle, 12-27.

Fissel, D.B. and Tang, C.L. 1991. Response of sea ice drift to wind forcing on the Northeastern Newfoundland Shelf. *J. Geophys. Res.*, **96**, 18,397-18,409.

Flato, G.M. and Hibler, W.D. 1989. The effect of ice pressure on marginal ice zone dynamics. *IEEE Trans. on Geoscience and Remote Sensing*, **27**, 514-521.

Madsen, O.S. and Bruno, M.S. 1986. A methodology for the determination of drag coefficients for ice floes. *Proceedings of the Fifth International Offshore Mechanics and Arctic Engineering Symposium*, American Society of Mechanical Engineers, New York, **4**, 410-417.

McPhee, M.G. 1978. AIDJEX Oceanographic Data Report. *AIDJEX Bullutin*, **39**, 33-78.

McPhee, M.G. 1979. The effect of the oceanic boundary layer on the mean free drift of pack ice: Application of a simple model. *J. Phys. Oceanogr.*, **9**, 388-400.

Mcphee, M.G. 1980. An analysis of pack ice drift in summer. *Sea Ice Processes and Models*, edited by R.S. Pritchard, University of Washington Press, Seattle, 62-75.

McPhee, M.G. and Smith, J.D. 1976. Measurement of the turbulent boundary layer under pack ice. *J. Phys. Oceanogr.*, **6**, 696-711.

Overland, J.E. 1985. Atmospheric boundary layer structure and drag coefficients over sea ice. *J. Geophys. Res.*, **90**, 9029-9049.

Savage, S.B. 1992. Marginal ice zone dynamics modelled by computer simulations involving floe collisions. Report for the contract 91-1547/5471, prepared for the IME of the National Research Council Canada.

Smith, S.D., Banke, E.G. and Johannessen, O.M. 1970. Wind stress and turbulence over ice in the Gulf of St. Lawrence. *J. Geophys. Res.*, **75**, 2803-2812.

Walton, O.R. and Braun, R.L. 1986. Viscosity and temperature calculations for assemblies of inelastic frictional disks. *J. Rheology*, **30**, 949-980.

5 A Friction Model Involving Shear Deformation of Individual Ice Floes

A tangential contact force model is introduced in the present chapter. It takes account of the elastic deformation that can occur because of the tangential contact forces. Simulations of inclined chute flows of a two-dimensional granular medium were conducted with the incrementally slipping friction force model, and with the Colombic model (cf. §3.3.1), in order to compare their performance. Finally, the numerical code used to simulate the dynamics of broken ice fields was modified to allow shear deformation of the individual ice floes and a study was performed to observe how this change affects the overall behaviour of the field.

5.1 Incrementally slipping friction force model

The tangential contact forces were modeled (cf. §3.3.1) using a Coulomb-type friction coefficient μ corresponding to the tangent of the static friction angle ϕ such that the friction force is $T = \mu N$, where N is the normal force. The particles were considered to be 'rotationally rigid' such that no shear deformation of the particles was possible in the tangential direction of the contact. The direction of the friction forces was found by evaluating the relative slip velocity, of the two particles, at their contact point. Since the tangential force normally tends to oppose the motion, it was considered to act in a direction opposite to the relative slip velocity. It can be easily demonstrated that this model is inappropriate for the *static case*. Consider for example a block having a weight W and resting on a bed inclined at an angle θ from the horizontal, where θ is smaller than ϕ. According to the Coulombic model, the tangential force applied on this block has a magnitude of $W \sin\phi$ and is acting upward along the plane. This computed tangential force is greater than the component of the weight along the plane and consequently could cause the block to move up the plane. In the following time step, the tangential force would have the same magnitude, but would act down the plane since the block has a velocity vector pointing in the opposite direction. This example illustrates that the above friction force model does not adequately simulate static and quasi-static flows of granular material. It also suggests that tangential contacts might not be properly treated in rapid flows.

This Coulombic friction force model will be replaced in the discussion that follows by the incrementally slipping friction force model of Walton and Braun [1986], which allows for shear deformation of the particles. The Walton-Braun (WB) model was based upon the studies of Mindlin [1949] and Mindlin and Deresiewicz [1953]. Their expression for the tangential force is for elastic spheres having an elastic Hertzian normal stress distribution in the contact regions. The friction force is a function of the tangential displacement. It increases in magnitude until the limiting value of μN is reached. A major assumption made by Mindlin is that the tangential displacement does not affect the Herztian normal stress distribution. Mindlin's expression for the tangential force T, for a sphere of radius R, as a function of the increment in tangential displacement, Δs, is as follows

$$T = \mu N \left[1 - \left(1 - \frac{16\, G\, a\, \Delta s}{(3(2-\nu)\mu N} \right)^{3/2} \right] \tag{103}$$

where G is the shear modulus, ν is Poisson's ratio, and a is the Hertzian contact radius corresponding to $(E^*NR)^{1/3}$, where E^* is related to Young's modulus through the expression $E^* = \frac{3}{2}(\frac{1-\nu^2}{E})$. The WB model is an approximation of Mindlin's model for spheres. The tangential force is evaluated using an effective tangential stiffness K_t associated with a non-linear spring. This parameter has an initial value of K_o and decreases with tangential displacement until it becomes effectively zero at full sliding, when $T = \mu N$. The tangential force is a history dependent quantity and is evaluated, for a time step $i+1$, as follows

$$T_{i+1} = T_i + K_t \Delta s \tag{104}$$

where K_t is given by

$$K_t = K_o \left(1 - \frac{T_i - T^*}{\mu N_i - T^*}\right)^\gamma \tag{105}$$

when the tangential displacement, for two contacting particles, starts taking place. The slip, Δs, which is the relative tangential displacement between two time steps, has a positive value in this direction causing T to increase. If the tangential displacement reverses direction, Δs becomes negative, T is reduced and the following expression for the tangential stiffness must be used

$$K_t = K_o \left(1 - \frac{T^* - T_i}{T^* - \mu N_i}\right)^\gamma. \tag{106}$$

When the tangential displacement reverses a second time, K_t is evaluated using equation (105). This pattern is continued for further reversals. In expressions (105) and

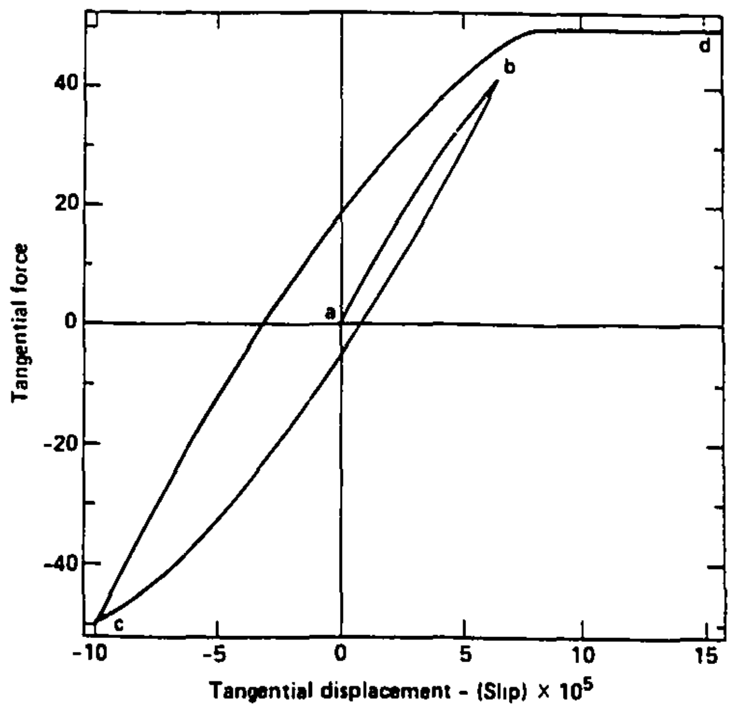

Figure 26: Tangential force generated by the incrementally slipping friction force model with a constant normal force and an ever increasing amplitude alternating tangential displacement ($\gamma = 1/3$) [Walton and Braun, 1986].

(106), γ is a constant parameter. According to Mindlin's theory $\gamma = \frac{1}{3}$, but it is mentioned in Walton [1992] that a value of 1 or 2 better simulates frictional contacts involving plastic deformation. Another parameter appearing in the last two equations is T^*, which is initially zero and takes on the value of T whenever the slip reverses direction. The graph of the tangential force versus displacement for a constant normal force is given in Figure 26. In the first segment of the curve which begins at the origin, T is increasing and equation (105) was used to evaluate the tangential stiffness. The tangential force is acting in a direction opposite to the relative slip velocity. In the second section of the curve where the slip has changed direction and the force is still positive, the force vector acts in the same direction as the relative tangential velocity until the point where T on the graph becomes negative. This section is associated with the recovery of tangential strain energy by the material during the rebound. When the slip reversed direction T^* took on the value of T calculated for this time step. For the following time steps T^* is scaled in proportion to the changes of N such that

$$T^*_{i+1} = T^*_i \left|\frac{N_{i+1}}{N_i}\right|. \tag{107}$$

The scaling of T^* is a compromise of Mindlin's theory in which the entire tangential force displacement curve scales with the normal force. With this scaling, changes of T are allowed when there is no tangential displacement. Walton and Braun [1986] have decided to check the tangential force against the limiting value of μN rather than scaling T this way.

The above model was checked for a simple two-dimensional static case. Following Walton and Braun [1986], the ratio of the initial tangential stiffness to the normal stiffness was chosen to be 0.8 and γ was arbitrarily set to 1. Twenty disks were dropped in an open box. The particles did not quickly come to rest, but instead the system became very agitated and at a certain point it virtually exploded, propelling the particles out of the box. After a detailed examination of the values calculated for the tangential forces it was observed that sometimes they would reverse direction suddenly and then have a magnitude of μN. This situation was found to occur when rapid changes of N, from one time step to another, took place. Negative values of K_t were then obtained due to the fact that T^*_i was scaled according to N to become T^*_{i+1}, whereas T_i was not modified. A solution to this problem was to scale T_i before calculating K_t in addition to T^*_i. When a tangential displacement occurs, T_{i+1} is

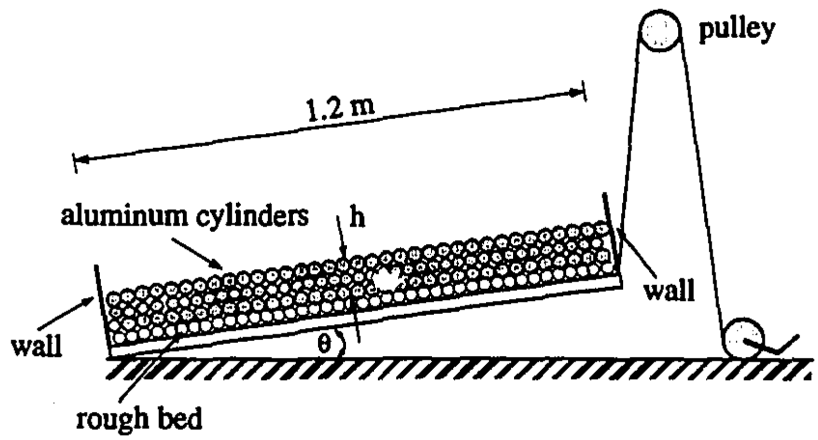

Figure 27: Experimental setup for the chute flows of aluminum cylinders.

evaluated according to the change in N but also according to the increment in slip, whereas T_{i+1} only depends on the variation of the normal force when Δs is zero. With this minor change, the static case described previously was properly simulated.

5.2 Inclined chute flows of granular material

Experiments involving aluminum cylinders piled on a rough bed were performed by Olivier Pouliquen in the Bulk Solids and Suspensions Laboratory at McGill and were subsequently simulated through molecular dynamics type computations. These experiments are considered to be two dimensional because there is no movement of the cylinders in the lateral direction and no side friction. The apparatus for this experiment is shown in Figure 27. The bed had a length of 1.2 m and a width of 8 cm. The rough surface consisted of plastic cylinders glued side by side on the bed and having a diameter of 2.5 mm. The aluminum cylinders were 6 cm in length. Half of them had diameters of 2 mm and the remaining half were 3 mm in diameter (mean diameter d=0.25 mm). At the two extremities of the bed the particles were constrained by two walls. The cylinders were initially arranged on the bed such that depth, h, was constant over the whole bed. A wire passing through a pulley was used to slowly raise one end of the bed. As the bed was inclined some local rearrangements of the cylinders occurred and at a specific moment practically all the cylinders flowed down the bed. This phenomenon will be referred to as an avalanche. The experiments were performed for $1, 2.5, 4, 7$ and 11 layers of cylinders. Each case was repeated 6 to 7 times for which the cylinders had different initial arrangements. The bed angles at which the avalanches were initiated were recorded and plotted against the number of cylinder layers in Figure 28. The effective static friction angles, ϕ, are found to increase with the reduction in depth of the granular material. The range of values of the recorded angles ('error bands') for a specific depth varies from 1° for 1 layer to 3° for a layer 3 particle diameters deep. On average, a range of 2.3° was obtained. These results are comparable to those that would be obtained with an infinitely long bed covered uniformly with cylinders because of the two end walls that were used.

5.2.1 Granular dynamics simulations of avalanches of aluminum cylinders

The experiment just described involves the transitions from static conditions to quasi-static and finally to a rapid flow of a granular material. The system is in static equilibrium when there is no movement of the particles, whereas the conditions are

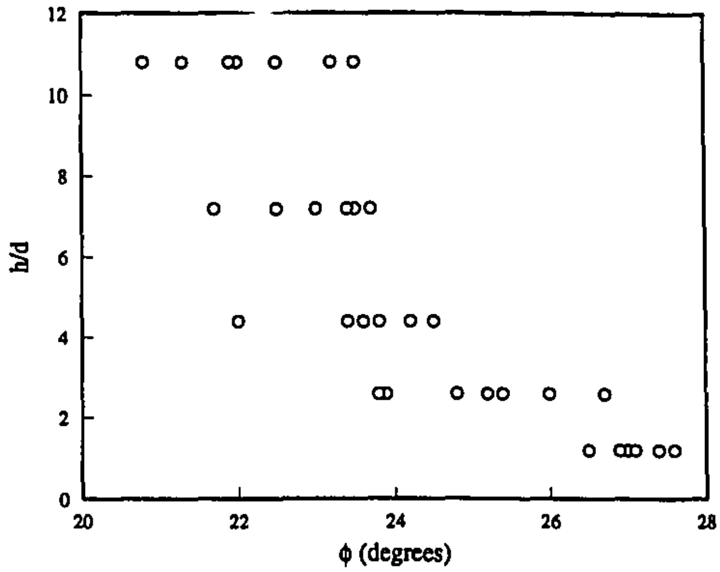

Figure 28: Effective static friction angles measured experimentally versus the nondimensional depth.

quasi-static when the particles are in a slow motion, when there is local rearrangement or just before the avalanche. The goal of these computations is to check the proposed tangential force model before rapid flow occurs. As noted previously, it was expected that the Coulombic tangential force model should fail during static or quasi-static conditions. This is what was observed when the experiment with aluminum cylinders was simulated with the Coulombic model. The simulations were more successful when the WB model was used to determine the friction contact forces. The numerical code used for the ice floe problem has been adapted to simulate the experiments with aluminum cylinders. The slight modifications made to the original code are presented below and they are followed by the computational results for the two types of simulations.

5.2.2 Problem formulation

The simulations of the above two-dimensional experiment were done using rough circular disks to represent the granular medium. The disks had a uniform random diameter distribution ranging from 0.6 D to 0.8 D, where D is the largest diameter encountered in the experiments. The reason why such a distribution was chosen, and not one of 2/3 D to D as in the experiment, is that a more stable initial arrangement was easier to obtain with this distribution. The external forces involved in the ice floe problem, i.e. air drag, water drag and the Coriolis force, have been replaced by gravity. The governing equation of motion for an individual cylinder is expressed as follows

$$m\frac{d\mathbf{u}}{dt} = m\mathbf{g} + \sum_{i=1}^{n}\mathbf{F}_i, \tag{108}$$

where m is the mass of the cylinder, t is the time, $\mathbf{g}$ is the gravitational acceleration and $\sum_{i=1}^{n}\mathbf{F}_i$ is the summation of the n forces arising from the particle's contacts with its neighbors. According to the nondimensionalization presented in Chapter 3, the gravitational acceleration, which has units of m/s^2, is nondimensionalized in the following manner

$$\mathbf{g}^* = \mathbf{g}\frac{M}{DK_1} \tag{109}$$

where D is the diameter of the largest cylinder and is therefore 3 mm; M is the mass of the largest cylinder corresponding to $\rho_{al} L\pi D^2/4$ and has a numerical value of 1.13 g since the density of the aluminum is 2.66 g/cm^3. The normal loading stiffness, K_1, was chosen to be 20 kN/m. This value is certainly less than the real one but it has been found that the various results that can be determined through numerical simulations, such as the stresses, are not too sensitive to the variations of K_1 as long as it remains within a certain range where it is sufficiently stiff. Besides, a lower K_1 permits the use of a larger time step since the contact time for a collision is inversely proportional to $\sqrt{K_1}$. With these values, g^*, the dimensionless gravity, is 0.0002. The latching spring force model is still used to evaluate the normal forces at contacts between cylinders. The energy dissipation associated with the normal direction of the contacts is related to a coefficient of restitution e which was set to 0.5. The unloading spring stiffness is found through equation (48), from which we can deduce that K_2 has a value of 80 kN/m. There is one material property which is left to define and it is the aluminum-aluminum friction factor μ. This parameter is required for both tangential contact force models. The value of μ was determined experimentally using two pairs of cylinders. In each pair the two cylinders are connected by two small sticks of equal length as illustrated in Figure 29. One set of cylinders is resting perpendicularly on the other pair which is initially horizontal and subsequently inclined. The angle at which the top cylinders start moving is the friction angle and it was measured to be 19.5°, corresponding to a factor of 0.355.

5.2.3 Simulation procedure

The bed is made up of 10 particles adjacent to each other and having a diameter of 2.1 mm. Periodic boundary conditions are applied in the eventual direction of the flow. The particles are initially arranged in a regular array and are given random velocity

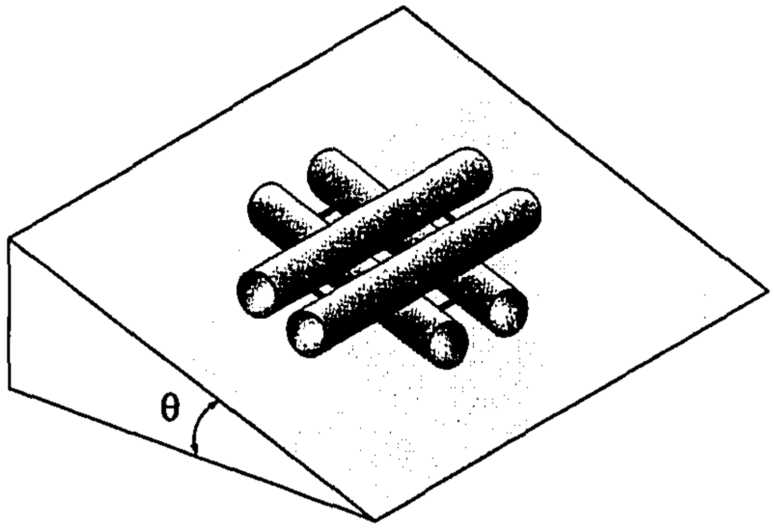

Figure 29: Experimental arrangement used to determine the aluminum-aluminum friction coefficient.

vectors. Under the action of gravity, they fall on the bed already inclined at 10° from the horizontal and then they flow downward for a short period of time until a quite stable arrangement is attained. After the particles have come to rest the bed angle is incremented at a rate of 5.9° per second. Animation software developed by Martin Serrer at NRC, Ottawa, was used to visualize the simulations. It has been a very useful tool to observe some behaviour or details that are difficult to detect from numerical results alone.

5.2.4 Results

The simulations were first performed with the earlier Coulombic friction force model for 5 and 7.5 layers of particles. The bed angles corresponding to the initiation of flow were approximately 19° for 5 layers and 17° for 7.5 layers. These results are not in agreement with the experimental data plotted in Figure 28, from which we can deduce that these angles should be around 23°. From the animations it was observed that the system was constantly agitated such that it was very difficult to say at which exact moment the avalanches took place. The particles were always flowing very slowly down the bed and sometimes they would move more rapidly and then stop.

With the use of the incrementally slipping friction force model, the behaviour of the particles from the beginning of a simulation up to the occurrence of the avalanche is in good agreement with the experiments. As the bed is raised there is no movement of the particles besides some local rearrangements similar to those observed during the experiments. The bed angles corresponding to the beginning of the flow were determined with a precision of 1°. For some trials the top layer would start moving, followed by the second and so on, all of which would take place in a relatively short period of time corresponding to a bed increment of 1°. For the majority of the cases studied, the whole system would fail within a time interval corresponding to an angle change of 0.25° after which all of the particles were in movement. In these simulations the ratio of initial to normal loading stiffness was 0.8 and γ was set to 1. The simulations were done for 1, 3, 5 and 7.5 layers of 10 particles and each case was repeated for several samples.

The static friction angles recorded from the simulations are plotted in Figure 30. As this graph illustrates, the numerical simulations properly reproduced the experimental behaviour. We can observe that there is a large scatter of the angles determined from the numerical simulations. This can be explained by the fact that a relatively small

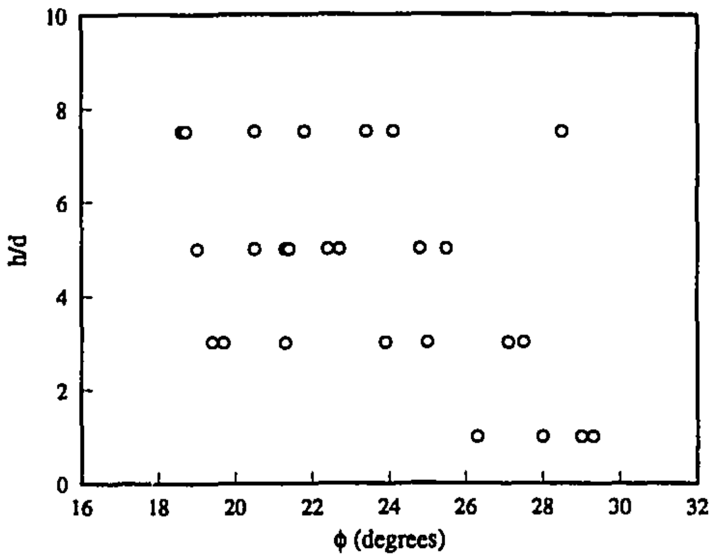

Figure 30: Effective static friction angles, observed numerically, versus the nondimensional depth.

number of particles was used in the simulations, such that when an unstable or a very stable region developed it had a significant influence on the whole system because of the periodic boundary conditions. Thus, low angles are due to the presence of a more unstable region whereas high angles are related to arrangements having a greater stability. The average values obtained numerically and experimentally are plotted in Figure 31. It appears from this graph that the two results have the same trend even though the numerical values become slightly lower than the experimental one as the depth of granular material increases.

5.2.5 Stress analysis

It is possible to treat a granular material as a continuum at length scales that are much larger than a particle diameter. On this basis, the equations describing the

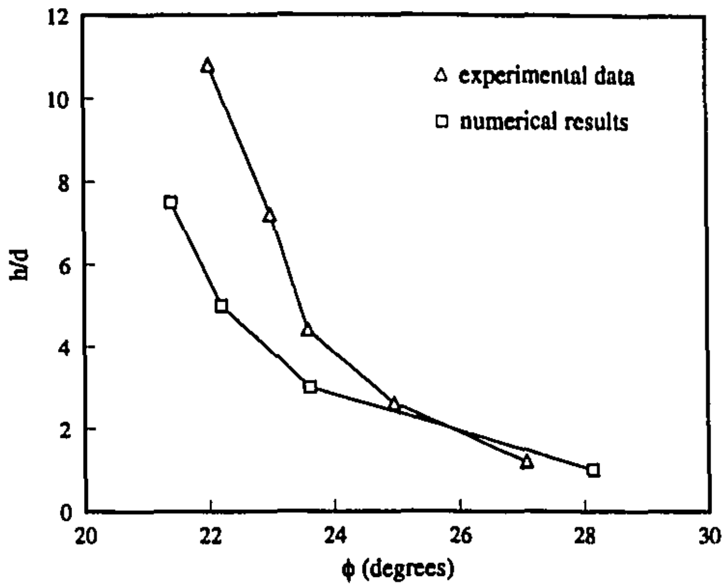

Figure 31: Comparison of experimental and numerical mean effective static friction angles versus the nondimensional depth.

stress variations in a medium inclined at an angle θ from the horizontal and having a density ρ are

$$\frac{\partial \sigma_{yy}}{\partial y} + \frac{\partial \tau}{\partial x} = \rho g \sin\theta, \tag{110}$$

$$\frac{\partial \sigma_{xx}}{\partial x} + \frac{\partial \tau}{\partial y} = \rho g \cos\theta. \tag{111}$$

In the case that we are studying, there is no stress variation along the bed, i.e. in the y direction, and thus the above expressions reduce to

$$\frac{\partial \tau}{\partial x} = \rho g \sin\theta, \tag{112}$$

$$\frac{\partial \sigma_{xx}}{\partial x} = \rho g \cos\theta. \tag{113}$$

These equations tell us that the stresses normal to the bed, as well as the shear stresses, should vary linearly with depth. In the course of granular dynamics simulations of a bulk solid it is possible to determine the instantaneous stress tensor acting over a surface V using the following relationship [Walton, 1992]

$$\mathbf{S} = \frac{1}{V} \sum_{j>i} \mathbf{f}_{ij} \mathbf{r}_{ij}. \tag{114}$$

The above equation evaluates the so-called *potential part* of the stresses due to the force transferred from a particle i to another particle j arising from the repulsive force $\mathbf{f}_{ij}$. The vector joining the two particles' centers is $\mathbf{r}_{ij}$. It is important when dealing with rapidly flowing granular material to also evaluate the kinetic contribution to the stresses which is related to the velocity fluctuations of the particles. In the present situation we are concerned with static or quasi-static conditions and thus this contribution is negligible. The four stress components, σ_{xx}, σ_{yy}, σ_{xy} and σ_{yx}, were calculated just before failure of the bulk solid occurred. This stress analysis was performed for two cases, trials (1) and (2), involving 5 layers of particles and for two other trials, (3) and (4), where the depth was of 7.5 particles. The width of the computational area, i.e. in the x direction, was divided into rectangular bands having a width of approximately 1 particle diameter and for which the four components of the stresses were calculated (Figure 32). The normal stresses σ_{yy} have strong fluctuations from one

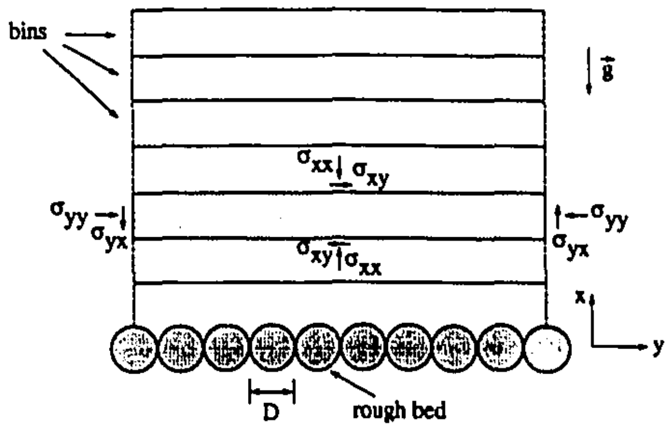

Figure 32: Stress components acting on a rectangular section.

bin to another. This is certainly related to the shape of the bin which is quite thin in the direction in which the σ_{yy} stresses act and thus the values calculated are not too accurate. The shear stresses, σ_{xy} and σ_{yx}, were found to be almost equal, as expected, for a symmetric stress tensor. The normal and shear stresses are plotted versus the depth of granular material in Figures 33 to 36. From these graphs we observe that σ_{xx} and σ_{xy} vary linearly with depth as expected. Linear regression was used to obtain equations fitting σ_{xx} and σ_{xy}. The ratio of the slopes of these equations was calculated for the four cases and were found to be very close to the tangent of the bed inclination. This is in agreement with the theoretical predictions of equations (113) and (114). The bed inclinations at which the stresses were computed for cases (1) to (4) and their corresponding theoretical angles are given in the following table.

bed inclination

measured	*theoretical*
(1) 20.5°	19.3°
(2) 22.7°	24.5°
(3) 20.5°	21.8°
(4) 20.5°	19.0°

Table 3: Comparison of the bed inclinations observed numerically with the theoretical angles evaluated from the stress components. Cases (1) and (2): 5 particle diameters deep; cases (3) and (4): 7.5 particle diameters deep.

Two conclusions can be drawn from these results:

· The use of the WB model to define the tangential forces developed at contacts between particles yields accurate values for the stresses.

· The static equilibrium equations appropriate for a continuum are found to accurately describe the stresses developed in a granular material made of a relatively small number of layers of particles.

5.3 Analysis of the effects of the incrementally slipping friction force model in simulations involving ice floes

Computations involving a rectangular array of 48 ice floes moving under the action of wind drag, water drag and Coriolis force were performed in order to study any difference that the incrementally slipping tangential model could produce. As the sketch of the computational box in Figure 37 illustrates, the ice floes were contained between two parallel rough boundaries of 8 particles each and by periodic boundaries along the other edge. All the particles were of the same size and had a diameter, D, of 7 km. A uniform geostrophic wind of 9.35 m/s was applied at various angles, ζ, from the right boundary and the turning angle was taken to be 22.5° for both atmospheric and

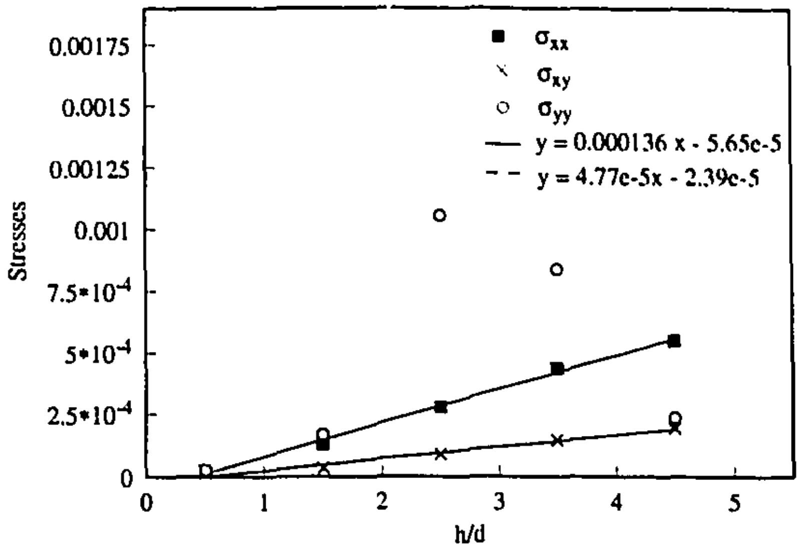

Figure 33: Stress components versus the nondimensional depth in a pile of 5 layers of particles, case (1).

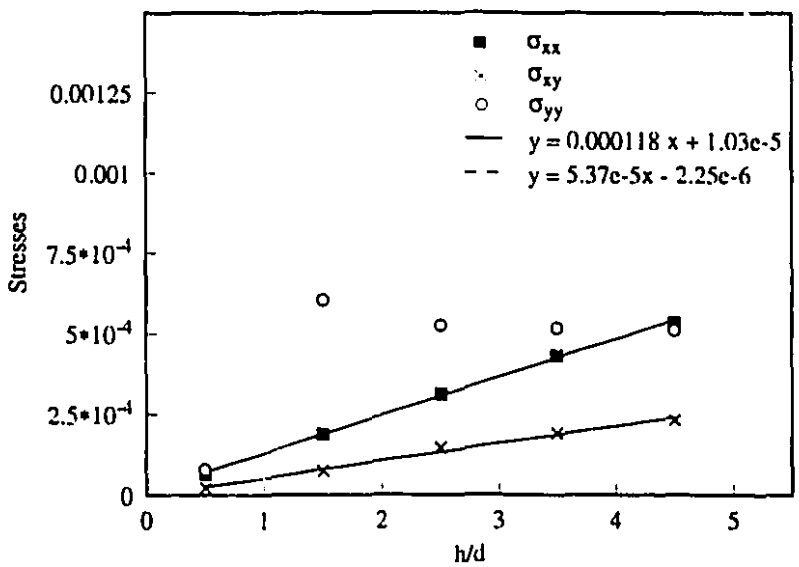

Figure 34: Stress components versus the nondimensional depth in a pile of 5 layers of particles, case (2).

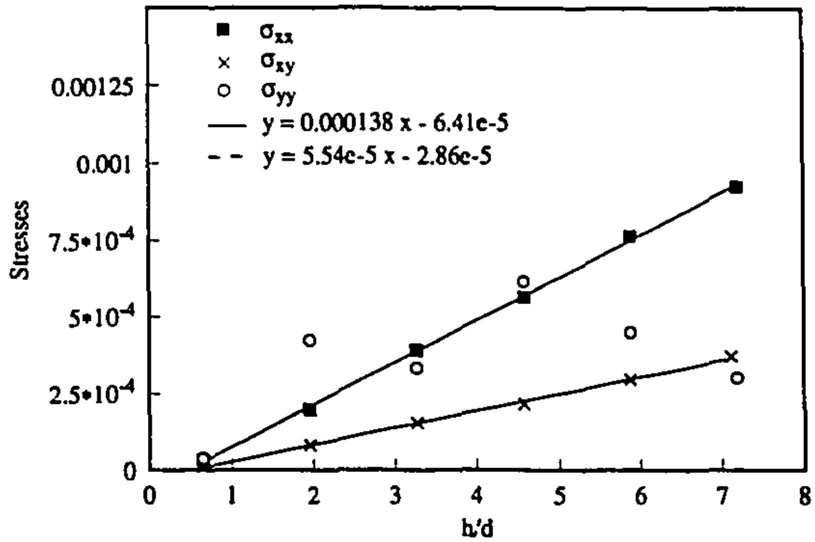

Figure 35: Stress components versus the nondimensional depth in a pile of 7.5 layers of particles, case (3).

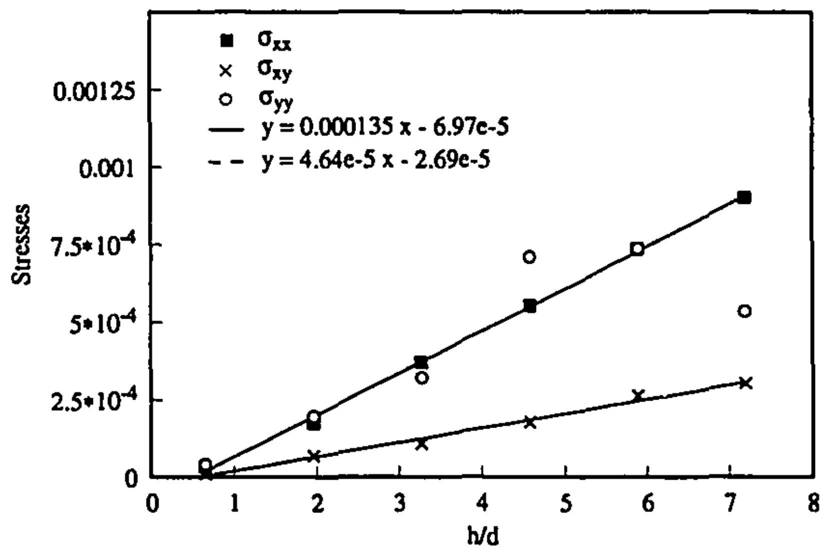

Figure 36: Stress components versus the nondimensional depth in a pile of 7.5 layers of particles, case (4).

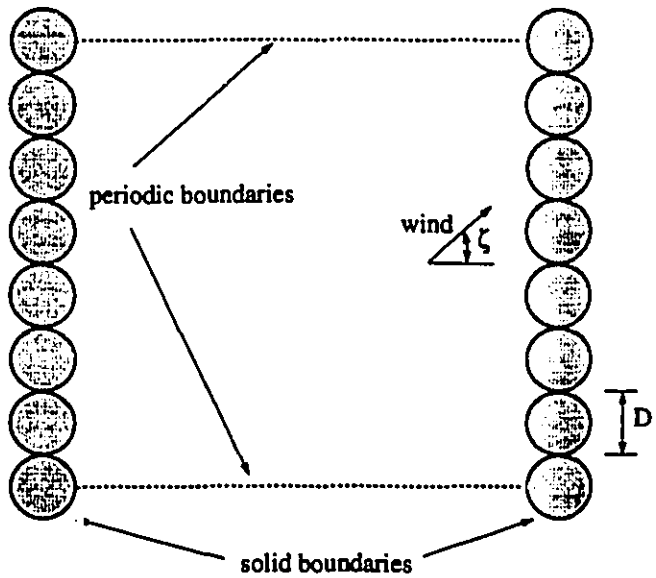

Figure 37: Computational box for ice floes simulations.

oceanographic boundary layers. The wind and water drag forces were evaluated from the linear relationships presented in Chapter 3. The coefficient of restitution was set to 0.5, the friction coefficient to 0.3 and the ice floes were considered to have a thickness of 1 m.

5.3.1 Observations and comparisons

Initially, each particle was given a small random velocity. Under the action of the wind, the floes started to flow and they were subsequently pushed by the Coriolis force toward the right solid boundary. The numerical results were processed by dividing the computational box into 9 bins for which velocities, concentrations and stresses were evaluated. The first step was to compare the long time averages of these variables. The resulting stress distributions are plotted in Figure 38 for a wind blowing parallel to the

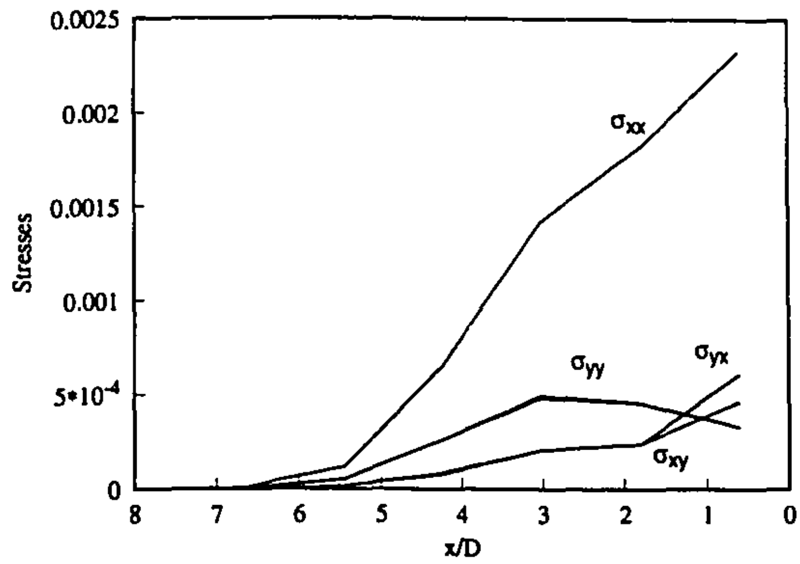

Figure 38: Average stress components versus the nondimensional distance from the right solid boundary, $\zeta = 90°$, turning angle=22.5°, D=0.7 km.

boundaries, and in Figure 39 for a wind inclined at 45°. From these graphs it is obvious that the average stresses, which were computed over 250,000 time steps, are nearly equivalent for the simulations performed with the WB model and with the Coulombic model. Cases involving two other wind angles, 25° and 65°, were also investigated and the stress distributions obtained were similar to those given in Figures 38 and 39. In all situations, velocity profiles and concentrations were found to be almost equivalent for the two models. These results have led us to investigate the instantaneous stresses generated by the two models. The σ_{xx} normal stresses, for the bin next to the wall, are plotted versus the time step, t, in Figures 40 and 41. The first graph is for a 90° wind and the second for a wind inclined at 45°. It is surprising how the stresses have the same trend even though the stresses computed for the simulations involving the Coulombic friction model fluctuate from one time step to another. We have demonstrated that,

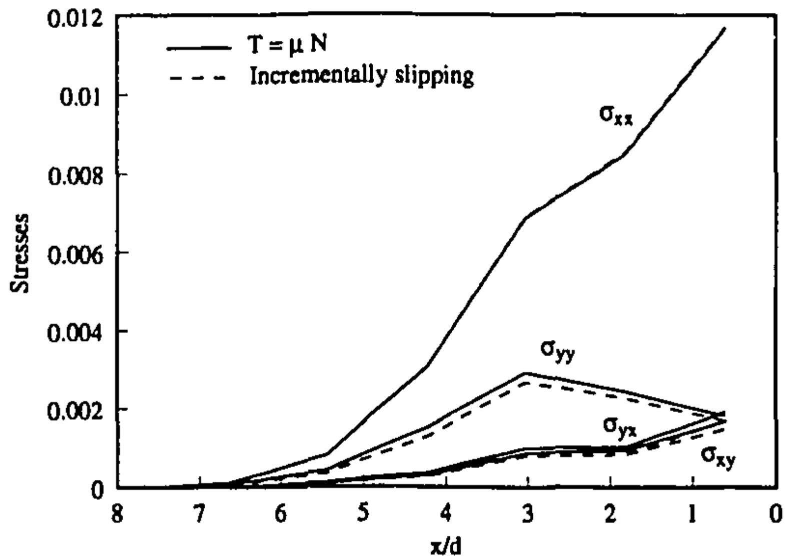

Figure 39: Average stress components versus the nondimensional distance from the right solid boundary, $\zeta = 45°$, turning angle=22.5°, D=0.7 km.

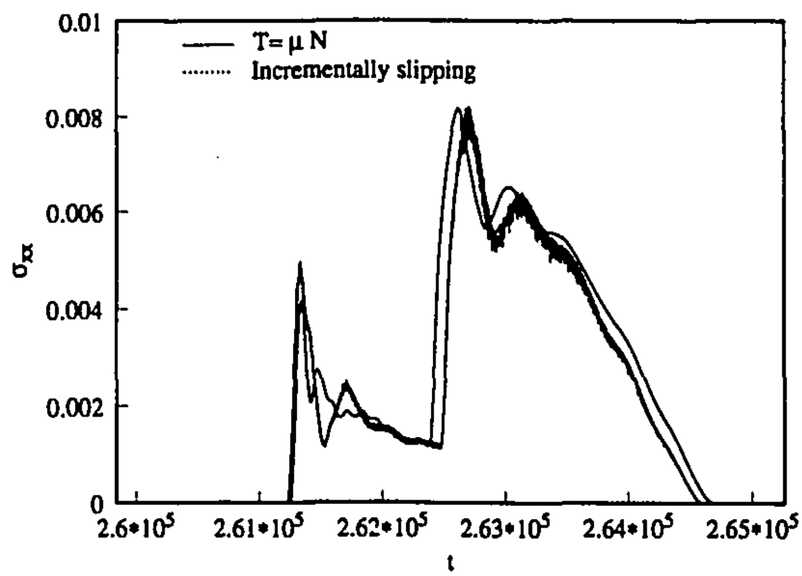

Figure 40: Instantaneous stress components versus time, $\zeta = 90°$, turning angle=22.5°, D=0.7 km.

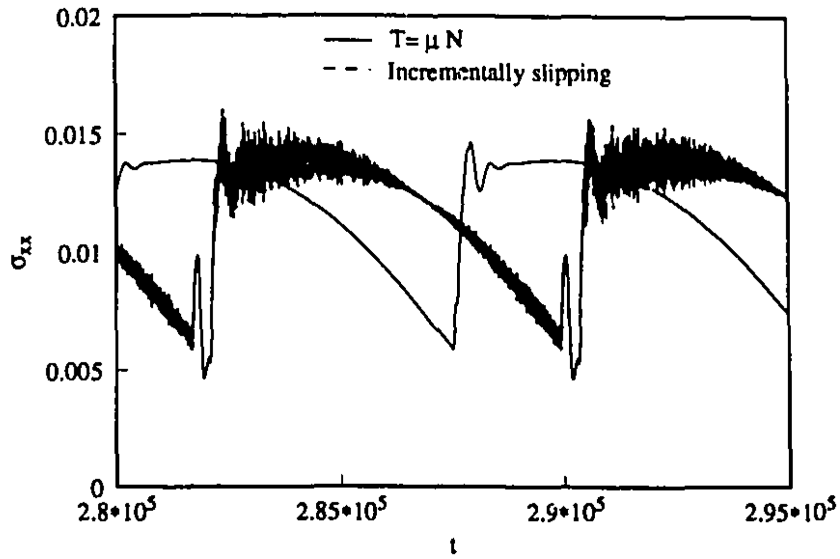

Figure 41: Instantaneous stress components versus time, ζ = 45°, turning angle=22.5°, D=0.7 km.

with the Coulombic tangential force model, the particles are constantly subjected to large tangential forces such that the stresses at a point or over an area of 1 or 2 particles are necessarily wrong. Spatial averaging over 1 bin, which contains approximately 8 particles, appears to be sufficient to smooth these variations and to yield stresses that are close to the exact values. The same behaviour was observed for the σ_{yy} and shear stresses and thus there is no need to present them. The reason the stresses are zero for a certain period of time when there is a geostrophic wind blowing parallel to the boundaries, is that the floes collect on the solid boundary and afterwards bounce back towards the interior region up to the point where they no longer touch, and finally the Coriolis force pushes them back toward the boundary.

The animation software was used to visualize the simulations, but no difference in the overall behaviour or in the development of the contact network was observed.

There was one exception, though, for the study case where the wind was inclined at 45° from the boundary. Indeed, it took 41,000 additional time steps, i.e. 36 hours in real time, for the ice floes to reach their steady flow configuration with the WB model. This difference is not negligible. It suggests that under transitional regimes the ice floes may behave differently, according to the friction force model, just as the cylinders did when they started to move at angles lower than expected when they were simulated with the Coulombic tangential model.

In order to further investigate the effects of the WB model, we made some computations to determine how much slip takes place between contacting particles. This was done by calculating the ratio of the tangential force to the normal force for approximately 100,000 contacts. The histogram obtained for a wind blowing parallel to the solid boundary is given in Figure 42. From this graph, we observe that only 27 percent of the contacts experience full sliding.

The same type of computation was done for a wind blowing at 45° from the boundary but for individual bins (Figure 43). The behaviour of a sample of non-uniform size floes, having diameters varying from 5 to 9 km, was examined for the same wind forcing. Slightly more slipping was found to occur with the non-uniform size distribution (Figure 44).

From these observations we can conclude that tangential forces implying shear deformation of the particles do not influence the behaviour of an ice field which is flowing under steady conditions. But, the results obtained with simulations involving aluminum cylinders suggest that we have to be careful with transitional regimes and also with static or quasi-static conditions. Such conditions may be developed by the

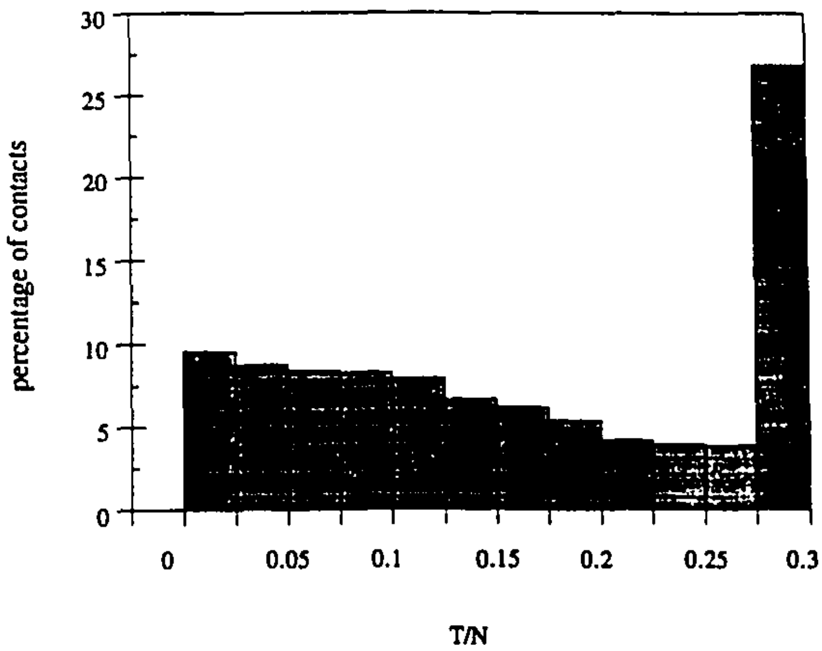

Figure 42: Histogram of the ratios of the tangential to the normal force, $\zeta = 90°$, turning angle=22.5°, D=0.7 km.

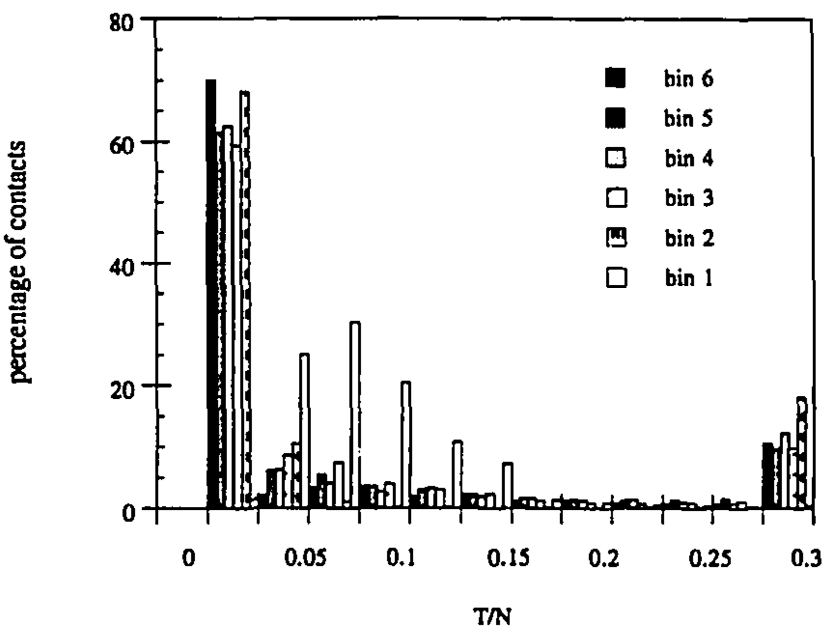

Figure 43: Histogram of the ratios of the tangential to the normal force for individual bins, $\zeta = 45°$, turning angle=22.5°, D=0.7 km.

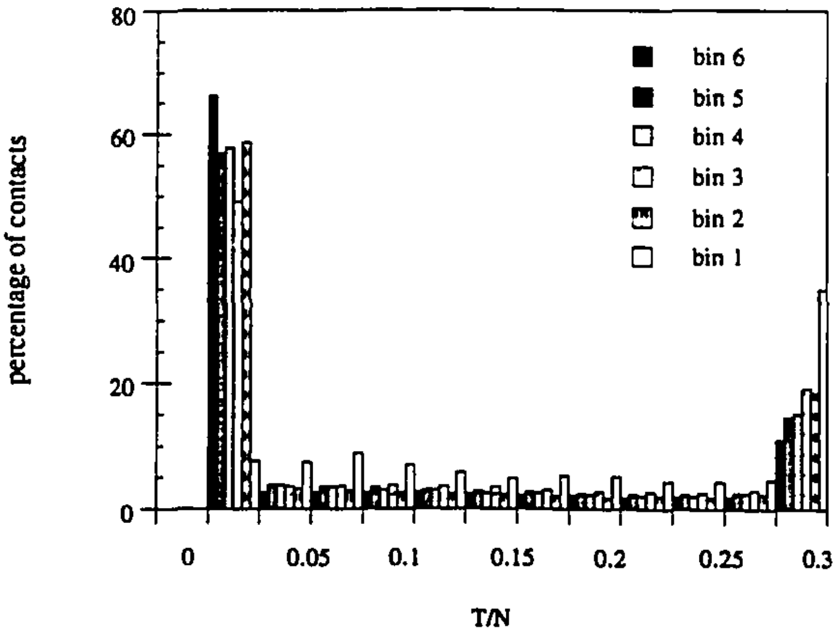

Figure 44: Histogram of the ratios of the tangential to the normal force for individual bins and for a non-uniform size distribution, $\zeta = 45°$, turning angle=22.5°.

presence of a drilling platform behind which ice floes collect and develop high pressures. The estimation of the forces generated by the ice cover on this platform by simulations conducted with the Coulombic model may very likely be wrong. It is suggested that further cases should be studied in order to determine the conditions under which it might be necessary to include an incrementally slipping friction force model in the numerical code which is currently being used.

5.4 References

Mindlin, R.D. and Deresiewicz, H. 1953. Elastic spheres in contact under varying oblique forces, *J. Appl. Mech. (Trans. ASME)*, **20**, 327-344.

Mindlin, R.D. 1949. Compliance of elastic bodies in contact. *J. Appl. Mech. (Trans. ASME)*, **16**, 259-268.

Walton, O.R. and Braun, R.L. 1986. Viscosity, granular-temperature, and stress calculations for shearing assemblies of inelastic, frictional disks, *J. Rheology*, **30**(5), 949-980.

Walton, O.R. 1992. Numerical simulation of inelastic frictional particle-particle interactions, *Particulate Two-Phase Flow*, edited by Roco, M.C., Butterworth-Heinemann, Boston, 884-907.

6 Summary and Conclusions

The development of a discrete element model for ice forecasting based on a granular dynamics approach is presented in this study. Some concepts of oceanography and of meteorology which are related to the motion of ice floes, such as the Ekman boundary layer and the turning angles, were reviewed. A discussion of the different kinds of forcing that govern the movements of ice floes based on field investigations was presented. The ice floes experience drag forces exerted by the wind and water currents. They are also subjected to a pressure gradient force resulting from sea surface tilt, to a Coriolis force, and finally to contact forces that arise from internal collisions. We have seen that ice floes can be treated as a granular material such that their movements and interactions can be studied by granular dynamics simulations. The details of the numerical model, which involves floe collisions and motion under the action of wind drag, water drag and Coriolis force, were given.

The non-linear effects of the wind and water currents on ice floe motion were studied and expressions for the drag forces were developed for circular ice floes. An equation was derived for the water drag force by numerically integrating the stresses, which depend on the square of the ice velocity relative to the water current, over the floe area. The rotational movements of the ice floes are resisted by the water shear stress at the bottom surface of the floe and, thus, an expression for the viscous torque was developed following the same procedure as for the linear drag force. The air drag force is given by an expression which has a relatively simple form since it relates the stresses to the square of the wind's velocity, the ice floe velocity being negligible. All these expressions require information that is calculated in the course of the simulations, such as the floes' linear and angular velocities as well as input parameters' values such as the wind's velocity, the water current, the floes' diameter, the drag coefficients and the boundary layers' turning angles.

The discrete element model has been modified in order to take into account the elastic deformation of the ice floes that occur because of the tangential contact forces. This was achieved by incorporating an incrementally slipping friction force model in the numerical code. In order to test the effects of this tangential force model, simulations of inclined chute flows of a granular material, in this case aluminum cylinders, were performed. More specifically, the transition from a quasi-static regime to a rapid flow was studied. The simulations were found to adequately reproduce the experimental behaviour. A stress analysis was conducted from which it appeared that the state of stress of the system can be accurately evaluated numerically. Simulations that were performed with the earlier Coulombic friction force model used in the ice floe problem yielded inadequate results. Subsequently, numerical simulations of a broken ice field, subjected to different wind conditions, were performed and an analysis was done in order to observe the effects of the incrementally slipping friction force model. The time average stress and velocity distributions were found to be nearly identical for simulations performed with the two tangential force models. The instantaneous stresses follow the same trend although those calculated when the Coulombic model was involved fluctuate strongly. Computations were performed to evaluate the ratio of the tangential force to the normal force in order to observe the amount of slip taking place at contacts between particles. For a geostrophic wind blowing parallel to the solid boundaries limiting the computational area, 27 percent of the contacts were found to experience full sliding. This value is lowered by 10 percent for a wind inclined at 45° from the boundary on which the ice floes collect. The above results are for floes having the same diameter. Slipping was found to increase significantly when the field consisted of floes having a non-uniform size distribution.